Title
Oxidation and Atmospheric Transformation of Vehicle Exhaust Particles

Author
Nguyen, Anh Nhat

Publication Date
2014

UNIVERSITY OF CALIFORNIA
RIVERSIDE

Oxidation and Atmospheric Transformation of Vehicle Exhaust Particles

A Thesis submitted in partial satisfaction
of the requirements for the degree of

Master of Science

in

Mechanical Engineering

by

Anh Nhat Nguyen

June 2014

Thesis Committee:
Dr. Heejung Jung, Chairperson
Dr. Guillermo Aguilar
Dr. Marko Princevac

The Thesis of Anh Nhat Nguyen is Approved:

Committee Chairperson

University of California, Riverside

ACKNOWLEDGEMENTS

I would like to express my deepest gratitude and sincere appreciation to my advisor, Dr. Heejung Jung. I am very fortunate to have him as my advisor. Without the nurturing atmosphere, strong encouragement and mentorship he has provided me over the years academically, this journey through graduate school would not have been possible. His diverse knowledge, effective teaching style, innovative idea and generosity make him a fabulous advisor, and more importantly, set the image of a great role model for me to follow. His guidance in leading me to become an independent learner, to question principles, to explore knowledge confidently on my own, and to be an articulate writer are the greatest gifts for my future endeavors in any occupations. Besides guiding me to succeed academically, he has shared with me many meaningful insights about life along with personal support and care during some of those toughest times. I cannot thank him enough!

I also want to give a special appreciation to Dr. Marko Princevac and Dr. Guillermo Aguilar for serving on my committee and imparting their knowledge onto me over the years as both an undergraduate and graduate student. I am thankful of Dr. Princevac insightful comments that helped to expand my knowledge in dispersion of emission, which have given significant improvement to my research. I would like to also thank Dr. Aguilar for always having an open door to questions and giving me a lot of help through the many classes I have taken with him.

I am very grateful of many colleagues at CE-CERT (Dr. Zhonging Zheng, Dr. Ehsan Hosseini, Dr. Manishkumar, Shrivastava, Haowei Wu, Dr. Shunsuke Nakao, Dr. Ping Tang, Yang Li, Liem Pham, Yue Lin, Eli Brewer, Desiree Smith) for being very resourceful in expanding my knowledge and perspective that have helped tremendously in the development of my research and this thesis.

At the end I would like to thank my family for their endless love, support, and encouragement. They have taught me to live a quality life by having perseverance, strength and commitment. During some of those darkest hours, they have given me tremendous amount of motivation and inspiration to keep pushing forward to achieve a successful life. Thanks Me Le, Ba Dan, Kai-Li, Me Dung and Bac Thanh, Ron……. Words cannot adequately express the gratitude I feel for everything they have done for me.

The text of this thesis, in part, is a summary of the author already published works that appeared in Kinetics of Soot Oxidation by NO_2 (*Environ. Sci. Technol. 2010, 44, 4796-4801)* and Interpretation of Secondary Organic Aerosol Formation from Diesel Exhaust Photo-oxidation in an environmental chamber *(Aerosol Science and Technology. 45. 964-972),* *Dedicated to my loving mother and father*

Le and Dan Nguyen

ABSTRACT OF THE THESIS

Oxidation and Atmospheric Transformation of Vehicle Exhaust Particle

by

Anh Nhat Nguyen

Master of Science, Graduate Program in Mechanical Engineering
University of California, Riverside, June 2014
Dr. Heejung Jung, Chairperson

Soot particles pose significant adverse health effects and influence on earth's temperature and climate. Hence, the elimination of soot emissions from diesel engines has attracted a lot of attention. Prior to this work, the investigation of soot oxidation is done mostly under air environment. However, since it is typical for NO_2 to be used in promoting regeneration under low-temperature soot oxidation for modern DPF, this study focuses on deriving the kinetics of soot oxidation under the influence of NO_2 being a major oxidant. An online aerosol technique of high temperature oxidation-tandem-differential mobility analysis is used with soot being oxidized in a laminar flow reactor at temperature ranging from 500 to 900℃ with NO_2 concentration from 0 to 600 ppm. The exposure of soot particles to the non-uniform temperature and NO_2 mixing ratio inside the furnace causing NO_2 thermal decomposition is thoroughly accounted for the first time. The soot oxidation rates being calculated as a function of frequency factor A_{soot} and activation energy E_{soot} are found to be: $A_{soot} = 2.4 \times 10^{-14}$ $nmK^{-0.5}s^{-1}cm^{3}molecule^{-1}$ and $E_{soot} = 47.1$ kJ mol^{-1}. NO_2 oxidation shows significantly lower activation energy when compared to that for O_2 at temperatures below 500℃. Even at higher temperature (800 to

900°C), the soot oxidation rates with NO_2 is still comparable to that with air. This indicates that NO_2 is a stronger oxidant than O_2 since only parts per million levels of NO_2 are sufficient to cause such significant soot oxidation.

After the emissions from diesel exhausts are released into the atmosphere, secondary organic aerosol (SOA) are formed from the photo-chemical oxidation of organic vapors and followed by gas-to-particle partitioning. This study aims to advance the understanding of diesel emission influences on SOA formation with a major focus on the photo-oxidation of aromatic hydrocarbons inside an environmental chamber that simulates atmospheric chemistry. The investigation through combining the real-time density measurement and other physical/chemical analysis (APM-SMPS, HR-ToF-AMS) demonstrates that mass-based measurement techniques are necessary for interpreting the physical processes (evaporation of SVOCs and condensation of secondary organic compounds) during SOA formation due to the external void space in the agglomerate particles. Analysis of O/C ratio has shown to increase rapidly from 0.05 to 0.25 within 12 hours inside the chamber, emphasizing that the multigenerational oxidation of volatile organic vapors from the exhaust to be an important source of SOA formation. The impact of different dilution methods on the diesel particles evolution inside the chamber is investigated for the first time. Lower effective densities and stronger evaporation of semi-volatile species is observed from the intense dilution by the ejector dilutor as opposed to the raw exhaust injection into a full bag inside the environmental chamber.

Table of Contents

List of Figures xi

List of Tables xii

Kinetics of Soot Oxidation.. 1

1.1 Introduction 1
1.1.1 Background.. 1

1.1.2 Soot Formation and Control in Diesel Engine Exhaust..................................... 2

1.1.3 Objective.. 4

1.2 Experimental Method 6
1.2.1 Diffusion Flame Burner.. 6

1.2.2 Dilution.. 7

1.2.3 HTO-TDMA System 8

1.3 Modeling 13
1.3.1 Temperature Profiles Modeling... 13

1.3.2 Modeling NO_2 Decomposition 14

1.3.3 Modeling the particle size decrease by oxidation.. 17

1.4 Result.. 19
1.4.1 Prediction of particle diameter decrease ΔDp 19

1.4.2 Oxidative and non-oxidative components of ΔDp... 20

1.4.3 TDMA particle size distribution after the furnace... 22

1.5 Discussion 24
1.5.1 Comparison with soot oxidation study: Case #1 24

1.5.2 Comparison with soot oxidation study: Case #2 24

1.5.3 Comparison with soot oxidation study: Case #3 26

1.5.4 Comparison of soot oxidation rate in the presence of air and NO_2 27

1.6 Conclusion... 29
Chapter 2 Interpretation of secondary organic aerosol formation from diesel exhausts photo-oxidation in an environmental chamber 31

2.1 Introduction 31
2.1.1 Background.. 31

  - 2.1.2 SOA from diesel exhaust ... 32
  - 2.1.3 Objective ... 34
- 2.2 Experimental Method ... 37
  - 2.2.1 Mezzanine chamber ... 37
  - 2.2.2 Analytical Instruments used for gas/particle analysis ... 38
  - 2.2.3 Dilution methods ... 44
- 2.3 Analysis of results from analytical instruments ... 46
- 2.4 Discussion ... 50
  - 2.4.1 Interpreting the formation of SOA ... 50
  - 2.4.2 Interpreting the effect of the dilution/injection method on the particulates' evolution inside the chamber ... 57
- Conclusion ... 64

References ... 66

List of Figures

Figure 1.1 Diffusion flame burner 6
Figure 1.2 Ethylene Flame.. 7
Figure 1.3 Air-Vac TD-110H vacuum transducer pump 8
Figure 1.4 Schematic of HTO-TDMA System 9
Figure 1.5 Alumina tube and quartz tubing in the furnace 10
Figure 1.6 Temperature Distribution at 0.6 Lpm and 600 ppm 13
Figure 1.7 NO_2 Concentration along the furnace.. 16
Figure 1.8 Predicted vs Measured NO_2 concentration... 16
Figure 1.9 Comparison of measured and predicted ΔDp 19
Figure 1.10 Variation of temperature, NO_2 concentrations, and soot oxidation rates 19
Figure 1.11 Size distribution from varying furnace temperature at a constant NO_2......... 22
Figure 1.12 Size distribution from varying NO_2 concentrations temperature of 800°C... 22
Figure 1.13 Comparison of soot oxidation rate in present study vs. rate by air. 28
Figure 2.1 Conception of diesel particulate matter (Maricq, 2007)................................. 32
Figure 2.2 Diesel particulate tri-modal size distribution 33
Figure 2.3 Schematic diagram of CE-CERT mezzanine chamber facility 37
Figure 2.4 Aerosol particle mass analyzer-scanning mobility particle sizer 39
Figure 2.5 Volatility Tandem Differential Mobility Analyzer 40
Figure 2.6 High Resolution Time-of-Flight Aerosol Mass Spectrometer 42
Figure 2.7 Various dilution methods for injection into the environmental chamber........ 44
Figure 2.8 Fractal Dimension 47
Figure 2.9 Particle volume concentration and mass concentration.................................. 50
Figure 2.10 Effective density... 50
Figure 2.11 Volume fraction remaining.. 51
Figure 2.12 Time series of effective density of particles (Run 5). 51
Figure 2.13 Time series of selected ions measured by an AMS for Run 1....................... 53
Figure 2.14 Mass spectrums obtained before and after UV irradiation for Run 1........... 54
Figure 2.15 Fraction of Organic Aerosols 56
Figure 2.16 Effective densities in an environmental chamber after injection 57
Figure 2.17 Evolution of bulk effective density 58
Figure 2.18 Comparison of transfer line concentrations before lights turned on 61
Figure 2.19 Evolution of primary organic aerosol fraction 62

List of Tables

Table 1.1 Flow rate of TDMA system 11
Table 1.2 ΔDp values at varying inlet NO2 mixing ratios and temperatures 20
Table 1.3 GMD decrease ratio (%) of carbon nanoparticles with various temperatures and NO2 concentrations for classified particle diameters of 41 nm and 81 nm..................... 25
Table 2.1 Analytical instruments used in the experiment.. 43
Table 2.2 Engine load, initial concentrations, calculated OH concentration, Df, bulk effective density, and overall dilution.. 46

Kinetics of Soot Oxidation

1.1 Introduction

1.1.1 Background

Soot is produced as an unwanted byproduct of incomplete combustion through many anthropogenic sources; for example, locomotives, fossil fuel burning, coal fired power plants, wildfire smokestacks, prescribe burns, biomass cook stoves and many other industrial sources are responsible for soot particles formation. Particularly, diesel engine is a significant contributor to the amount of soot released into the atmosphere. As the amount of diesel fuels injected per cycle is increased to produce more power, the problem with air utilization during the combustion process leads to the formation of excessive amount of soot. Consequently, these soot particles cannot be oxidized fast enough and get released as pollutants during the exhaust stroke. Even though such incomplete combustion due to heterogeneous fuel/air ratios for on-road vehicles leads to high soot formation, diesels are still widely used in heavy duty applications due to their excellent fuel economy and durability.

Soot has major influences on earth's climate and public health risk. During the process of soot formation, Polycyclic Aromatic Hydrocarbons (PAHs) precursors are inevitably produced as an intermediate. Besides being carcinogenic, PAHs are considered hazardous to the lungs and can cause severe respiratory problems. Hence, this attributes significantly to the poor air quality in Los Angeles Basin where a child being born has a great chance of inhaling more extremely toxic and cancer-causing pollutants in the first two weeks of his/her life than the EPA (Environmental Protection Agency) considers safe for a lifetime (Claire, 2004). From an environmental perspective, soot coats the snow and ice surfaces inducing the albedo perturbation, which in turn increases the sunlight absorption characteristics. Thus, soot particles have been shown to be second only to carbon dioxide in its global warming contribution and acceleration in the melting of ice glaciers (Hansen, 2004). In addition, soot which is predominately composed of black carbon has the property of cutting off sunlight to a greater degree than many other substances. As a result, the dark soot clouds have the potential to decrease the duration of sunshine over many large cities by 17% (Hansen, 2004). Heavy fog is another critical visibility consequence. The oily tar in the soot creates a protective film over the outside of the drop to prevent the fog from fast evaporation, making it denser and thicker than country fog (Seinfield, 2006). Indeed, the California Regional Haze Plan control strategy is developed to reduce anthropogenic emission sources, including rigorous controls for stationary and mobile sources, to reach visibility goals and pristine air by 2018 (CARB, 2014).

1.1.2 Soot Formation and Control in Diesel Engine Exhaust

Soot particles are formed on the fuel rich side of the reaction zone after passing through the inception zone at approximately 1700K inside the engine cylinder (Stanmore, 2001). Depending on the fuel chemistry and flame residences time, not all the soot formed in the flame can be oxidized after passing through the high temperature oxidation zone. The turbulence flame condition inside the engine combustion chamber causes the formation of soot wings, which allow the non-oxidized soot to break through the flame and be perceived as smoke.

After 1987, many strict regulations for diesel engine emissions were established (Felton, 2001). In order to satisfy the criterion of these regulations, two approaches from the internal and external engine measures are used to control the soot emission from the vehicles. Soot particles could be reduced through two methods:

1) Modifying the combustion strategy inside the engine to become more efficient

2) Effectively removing soot from the exhaust stream using diesel particulate filters

By 2007, EPA has passed a heavy-duty engine standard such that all on-road diesel must have diesel particulate filters (DPF). Since the DPF has a finite capacity, it must be continuously or intermittently regenerated by catalytic soot oxidation to prevent severe blockage and overfill causing damage to the engine through excessive exhaust back pressure. Passive or active catalytically coated DPF can be used for removing the trapped soot. Passive DPF allows continuous regeneration in the absence or intervention of engine management system. In urban traffic with low loads, active regeneration is preferred to burn off soot through a targeted high exhaust gas temperature controlled by the engine management system. The worldwide leading DPF system is the continuously regenerating trap (CRT) from Johnson Matthey, which installs an oxidation catalyst in front of the filter to generate the necessary nitrogen dioxide required to keep the filter clean (Zhang, 2010).

The DPF regeneration must be done under the lower temperature range to avoid thermal fatigue of the devices and to minimize the energy demanded for regeneration (Shrivastava, 2010). Besides containing N_2, O_2, CO_2, CO, PAHs, SO_x and other metals, NO_2 is also presence in the exhaust at a typical amount of 5 to 15% of the total NO_x. However, this NO_2 mixing ratio is increased to 50% due to platinum catalysts that oxidize NO to NO_2 in the temperature range of 300 – 350℃ (Marques, 2004). In order to achieve effective regeneration, a detail analysis of soot oxidation mechanism within the cylinder or exhaust after-treatment system in the presence of NO_2 and O_2 is necessary.

1.1.3 Objective

Although there have been former studies on soot oxidation, this current study contains many advantages. It has been shown that the reaction rates of soot oxidation for N_2O, NO, O_2 are approximately equivalent but are not as prominent as for NO_2 (Stanmore, 2008). In other words, NO_2 is a stronger oxidant in lowering the activation energy of oxidation than O_2, especially under the low temperature range of 200-500℃ (Ehrburger, 2002). Also, NO_2 is a very critical component for the chemical processes within the diesel CRT and can potentially increase soot oxidation through acting synergistically with O_2 (Setiabudi, 2004). Despite the importance of NO_2, many former studies (Stanmore, 2001; Higgins, 2002; Nienow, 2005) were done in the absence of it.

Many previous studies (Setiabudi, 2004; Jacquot, 2004; Kamm, 2004) have used thermo-gravimetric analysis (TGA). Since TGA is an offline method, it has the consequences of soot aging due to the time elapsed between sample collection and data analysis. Also, it is very difficult to decouple heat from mass transfer effect for soot collected on a substrate. These are both dependent and coupled non-linear processes which make the quantification of kinetics of soot oxidation very challenging. As the particles shrink from oxidation, the heat transfer varies due to the changes in the packing gaps between the particles. The mass transfer of oxidized soot is more efficient for online method such as a flow reactor by preventing diffusion limitation and ensuring that each particle is suspended in a heated environment. Therefore, the oxidation kinetics that is derived based on TGA can be biased due to these limitations. A possible method to minimize these issues is using the online aerosol technique of high temperature oxidation-tandem differential mobility analysis (HTO-TDMA) (Nienow, 2005).

In order to overcome all of these disadvantages, the kinetics of soot oxidation is investigated in this study with NO_2 being the primary oxidant and using the online method, HTO-TDMA. The work is done under N_2 environments with NO_2 inlet mixing ratios ranging from 0-600 ppm. The complication of the experiment arises since NO_2 will inevitably decompose at high temperature. Therefore, the kinetic parameters for soot oxidation are derived as a function of non-uniform NO_2 concentration and temperature along the axial of the furnace. The furnace temperature is set between 500-950℃ since it is not possible to record any significant changes in particle size at the lower temperature range of 200-500℃ due to the limitations from the instruments. Nonetheless these kinetics data at the higher temperature range are still very valuable since the temperature within the cylinders of diesel internal combustion engines varies from 500-2000℃.

1.2 Experimental Method

1.2.1 Diffusion Flame Burner

In this experiment, ethylene (C_2H_4) is used as a fuel substitute for diesel engine to generate polydisperse soot particle in the diffusion flame burner as shown in Figure 1.1. The core of the burner is a 9 ½ inch long tubing with a diameter of 9.5 cm located at the center of a stainless steel cylinder. Ethylene is sent through that inner core circular tube at 128 cc per minute together with a peripheral airline connected to the bottom of the outer cylinder. Stack of beads and meshes are installed between the core and outer cylinder. After the air passes through this, it enters the honeycomb to form the surrounding co-flow air, which is set at 50 liters per minute, and diffuse with the gaseous fuel from the core for flame ignition. Particles are sampled through a 1 mm orifice drilled at the bottom of a horizontal 11 mm inner diameter stainless steel sampling tube.

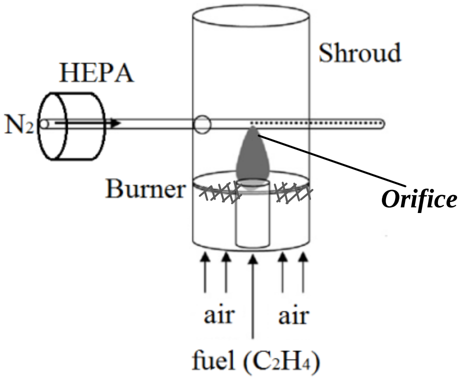

Figure 1.1 Diffusion flame burner

The tip of the flame as seen in Figure 1.2 is maintained at a 5 cm in height such that it slightly touches the orifice to ensure stable sampling condition. In order to prevent the flame from fluctuation and to minimize disturbance from outside air current, two cylindrical glass shrouds are stacked perfectly on top of the outer cylinder and sealed with an aluminum foil on the outer wall of each slot to cover the breach. The glass cylinder on the top is 27.8 cm in height and glass cylinder at the bottom is 9 cm in height.

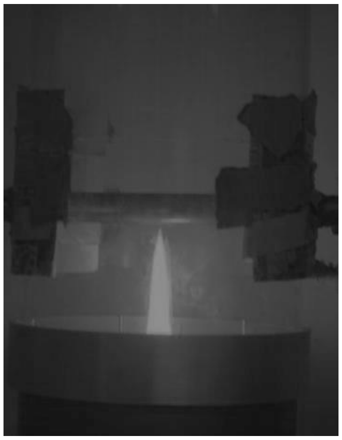

Figure 1.2 Ethylene Flame

1.2.2 Dilution

After the soot particles are collected into the sampling probe, they are diluted and quenched by a constant N_2 gas flow of 5 liters per minute. A HEPA filter is attached to one end of the sampling probe to prevent contamination of the sampling process by the entrance of particles from the environment. The sampling line is then connected to the Air-Vac TD-110H vacuum transducer pump as shown in Figure 1.3 such that it further dilutes the soot particles from the flame. When compressed N_2 at 30 psi with flow of about 20 liters per minute is sent into the inlet of the ejector dilutor, a vacuum flow of 6.2 liters per minute is created. Hence, this produces secondary dilution when the soot is passed through the orifice placed at the vacuum end of the ejector.

Such dilution helps to prohibit the soot from further accumulation to form agglomerates; fractal-like agglomerates can complicate the kinetics modeling. In addition, it is necessary to dilute the soot in prevention of exceeding the concentration limit of 10^5 particles/cc for the condensation particle counter (CPC).

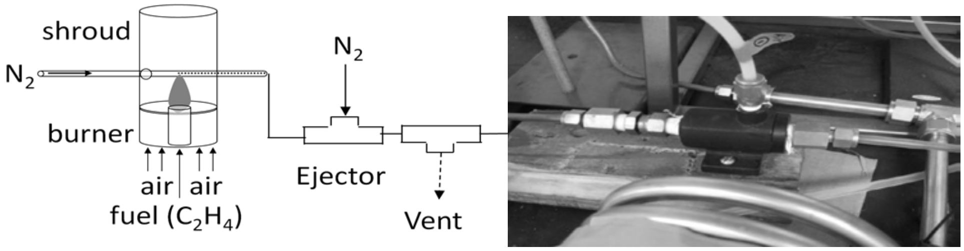

Figure 1.3 Air-Vac TD-110H vacuum transducer pump

1.2.3 HTO-TDMA System

The HTO-TDMA system in Figure 1.4 is used to first select the desired size of the soot particles and then scan the size distribution after the soot are oxidized through the furnace. Before entering the DMA-1, the aerosol particles must pass through a ½ inch stainless steel tubing with 7 concentric turns, in which the total length of the mixer is longer than ten times the tube diameter. This ensures the flow inside the tubing is laminar and the gases are mixed thoroughly. The carrier gas N_2 (purity 99.999% Praxair) is mixed with NO_2 (certified at 5049 ppm) in different proportions to get the desired mixing ratio of NO_2 ranging from 0-600 ppm, which is constantly monitored by a Horiba PG-250 Portable Multi-Gas Analyzer before entering the sheath flow of DMA-1 to avoid disturbing the aerosol flow.

As seen in Figure 1.4 the sampling line must pass through the neutralizer (radioactive source: Polonium-210) before entering DMA-1. The neutralizer emits alpha particles (α) and ionizes the surrounding atmosphere into positive and negative ions. By passing through the neutralizer, the particles acquire charges from colliding with the ions. This will in turn establish a known Boltzmann equilibrium charge distribution that can relate the dependency of the charges and sizes of the aerosol particles. Hence, a unique electrical mobility can be assigned to every particle size.

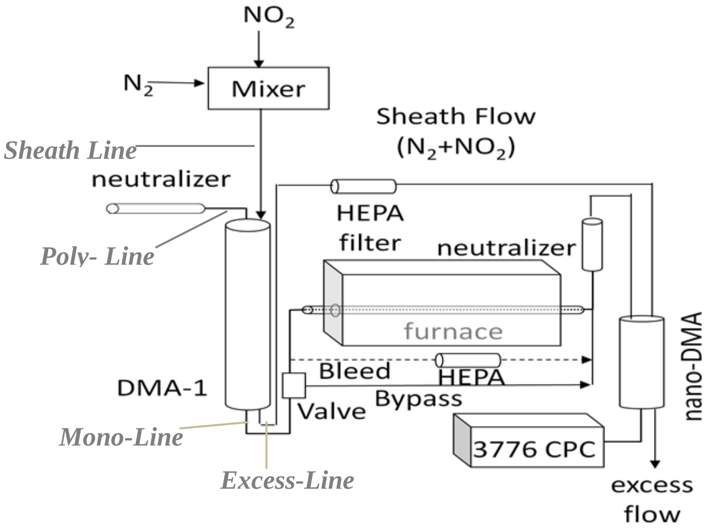

Figure 1.4 Schematic of HTO-TDMA System

The DMA-1 consists of a grounded outer cylinder and a central rod where a voltage is applied to select the corresponding particle sizes. The DMA works on the principle of balancing between the electrostatic and Stokes drag forces, which are both perpendicular to the direction of aerosol flow. Particles that are smaller and/or have a higher charge than the desired ones will settle in the upstream of the central rod due to obtaining higher electrical mobility values. On the other hand, the larger and/or uncharged particles having lower mobility will pass out of the DMA through the excess line. Hence, this allows only those particles with the desired electrical mobility to pass through the slit at the end of the central rod.

The NO_2 sheath flow mixes with the polydisperse aerosol line and are sent through DMA-1 (TSI 3081 series long column DMA) where monodisperse particles of 40 nm in sizes are selected based on electrical mobility. Calculations indicate that with sheath and aerosol flow rates of 10 and 1 liter per minute, respectively, will allow complete, homogeneous mixing. TEM images of soot nanoparticles from ethylene diffusion flame in previous studies have shown to be roughly spherical in shape for size range between 30-60 nm and the fundamental unit of soot agglomerates are spherules with diameter of 10-50 nm (Nienow, 2005). If particles with size smaller than 40 nm are chosen, loss in sensitivity of measurements will occur at higher temperatures and NO_2 mixing ratios. Therefore, the size of 40 nm is chosen for particles selection in order to model the particles as roughly spherical to simplify the kinetic analysis and also for comparison with former research works.

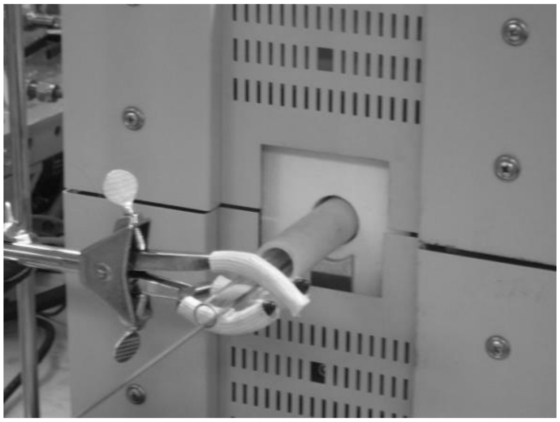

Figure 1.5 Alumina tube and quartz tubing in the furnace

The size-selected monodisperse line is then oxidized in a quartz flow tube placed at the center of a high temperature flow reactor (LINDBERG/BLUE M Model HTF55122A single zone tube furnace) as shown in Figure 1.5. The quartz tube is surrounded by an alumina tube to provide a uniform heat flux to the particle inside the tube (Higgins, 2002). The length of the exterior of the furnace is 21 inches and the heated length is 12 inches (LINDBERG/BLUE M user manual). The oxidation is conducted at various furnace set-point temperatures ranging from 500-950℃.

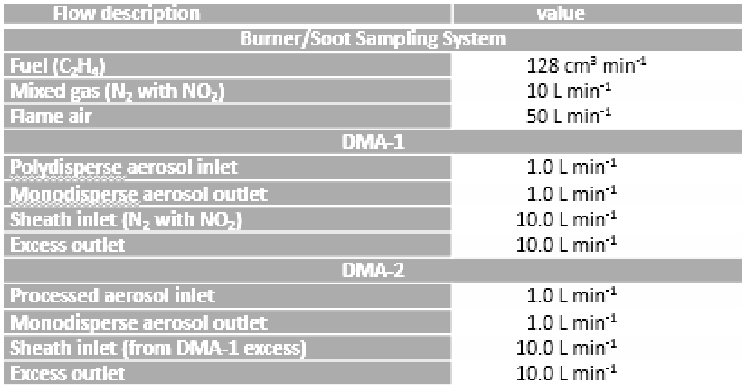

Flow description	value
Burner/Soot Sampling System	
Fuel (C_2H_4)	128 cm^3 min^{-1}
Mixed gas (N_2 with NO_2)	10 L min^{-1}
Flame air	50 L min^{-1}
DMA-1	
Polydisperse aerosol inlet	1.0 L min^{-1}
Monodisperse aerosol outlet	1.0 L min^{-1}
Sheath inlet (N_2 with NO_2)	10.0 L min^{-1}
Excess outlet	10.0 L min^{-1}
DMA-2	
Processed aerosol inlet	1.0 L min^{-1}
Monodisperse aerosol outlet	1.0 L min^{-1}
Sheath inlet (from DMA-1 excess)	10.0 L min^{-1}
Excess outlet	10.0 L min^{-1}

Table 1.1 Flow rate of TDMA system

As seen in Figure 1.4, a parallel bypass line is added to periodically monitor the flow rate of the monodisperse particle stream from DMA-1 such that a constant value is always maintained throughout the experiment. Furthermore, according to Table 1.1 (reporting a summary of the TDMA flow rates), the monodisperse aerosol flow from DMA-1 to the furnace was originally maintained with a laminar flow element at 1 liter per minute. However, this volumetric flow rate has been shown through many experimental runs to have negligible decrease in the particle diameter as a function of the various NO_2 concentrations and furnace temperatures. As a result, the flow rate of the monodisperse line after DMA-1 in Table 1.1 is reduced to 0.5 liter per minute by bleeding 50% of the mono-line to bypass the furnace and followed by re-mixing with the main flow exiting the furnace. This method helps to increase the sensitivity of the soot oxidation measurements by allowing the soot to have additional residence time inside the furnace.

The resulting oxidized particle size distribution from the high temperature flow reactor is obtained by using the nano-DMA (TSI 3085 series nano-DMA) with an Ultrafine Condensation Particle Counter (UCPC) as the detector. This nano-DMA is designed to reduce particle losses of nanoparticle and improve size resolution in the range of 3-50 nm (Chen, 1998). The HEPA filtered excess line from DMA-1 is used as the sheath flow of the nano-DMA. The SMPS software is used to control the high voltage supplier (Bertan 602C) such that the voltage on the center electrode of the nano-DMA continually changes to scan for different particle sizes corresponding to the varying voltages. The Ultrafine Condensation Particle Counter (TSI Model 3776) is an ideal instrument for particle with size less than 20 nm. The UCPC uses butyl alcohol, (C_4H_9OH), as a working fluid. Once the supersaturated alcohol vapor is cooled after the saturator, it will condense onto the existing nuclei of aerosol particles and form droplet large enough to be detected by the optics.

1.3 Modeling

1.3.1 Temperature Profiles Modeling

The temperature in the furnace is found to be non-uniform; it reaches a maximum value near the middle of the heating section but decreases to room temperature at the two ends of the furnace. Therefore, it is necessary to derive the temperature distribution in the quartz tube at 0.5 liter per minute for the various furnace set point temperatures between 500-950℃ with an Omega Type-K exposed-tip thermocouple. To ensure that the tip of the thermocouple is at the center of the quartz tubing, a home-made tripod is added. The average is taken from the 11 temperature measurements along the horizontal direction (both upstream and downstream) of the furnace.

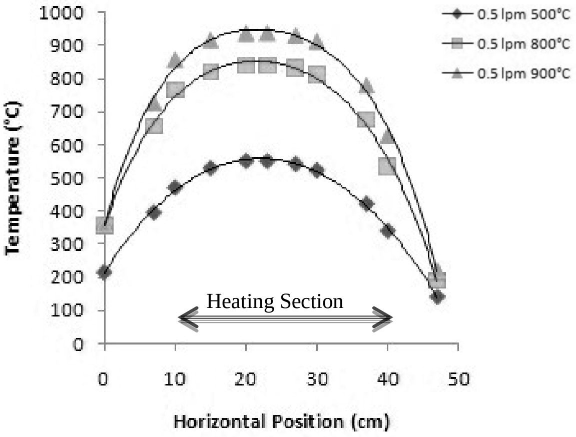

Figure 1.6 Temperature Distribution at 0.6 Lpm and 600 ppm

A fourth order polynomial fit is used to model the temperature profile along the various horizontal locations throughout the furnace. Figure 1.6 shows the measured temperature profile at the furnace set-point temperature of 500℃, 800℃ and 900℃. As expected the temperature is the highest and considerably steady in the middle of the furnace heating section. This distribution from the temperature fitting gives a more accurate temperature reading at any axial location along the furnace, which is a necessary parameter used during kinetics computation for soot oxidation and NO_2 decomposition.

1.3.2 Modeling NO_2 Decomposition

From a Gibbs free energy analysis of NO_2 balanced in N_2 carrier gas (Eq. 1- Eq. 2), it is apparent that NO_2 decomposes to NO spontaneously as a function of temperature and residence time within the furnace at a temperature higher than 510℃. Therefore, in order to compute the soot oxidation kinetics accurately, an NO_2 decomposition analysis must be made to obtain the accurate NO_2 concentration at any location along the furnace.

$$\mathbf{NO_2 + NO_2 \rightarrow\ O_2 + NO + NO} \qquad \text{Eq. 1.1}$$

$$\mathbf{\Delta G = \Delta H - T\Delta S} \qquad \text{Eq. 1.2}$$

$$where\ \Delta H = 114.18\frac{kJ}{mol}, \Delta S = 146.5\frac{J}{mol\ K}$$

Instead of using the NO_2 concentration from the sheath line to model the thermal decomposition, the NO_2 is actually read from the aerosol line before and after the furnace to get a more direct result. The NO_2 mixing ratios are measured by increasing the temperature at the inlet from 500 to 950℃ and NO_2 mixing ratio from 200 to 600 ppm.

The decomposition of NO_2 is known to be a second order reaction. The rate constant for Eq. 1.1 is achieved with the empirical Arrhenius rate expression (Eq. 1.3).

$$\mathbf{k(T) = A_{NO_2}exp\left[-\frac{E_a}{RT}\right]} \qquad \text{Eq. 1.3}$$

where k(T) is the second-order rate constant in $cm^3\ molecule^{-1}s^{-1}$, A_{NO2} *is the frequency factor, and* E_{NO2} *is the activation energy.*

When the second-order rate law for NO_2 is integrated, a relation between the initial and final concentrations of NO_2 with respect to time can be derived as in Eq. 1.4. This form of keeping the exponential coefficient of the rate equation as a constant in the derivative is the most common usage in reviewed literature, table of rate constants and simulation software.

$$\mathbf{\frac{1}{N_t} = 2k(T)t + \frac{1}{N_0}} \qquad \text{Eq. 1.4}$$

where N_t *is the* NO_2 *concentration at any given axial location in* cm^3 *molecules*$^{-1}$ s^{-1} *,* N_0 *is the initial* NO_2 *concentration at the furnace inlet when time is zero, t is the time in seconds spent by particles up to the location of interest.*

The values of E_{NO2} = 116 kJ mol^{-1} (activation energy) and A_{NO2} = 7.49 x 10^{-12} cm^3 $molecule^{-1}$ s^{-1} (frequency factor) have been found experimentally by Park et al. (Park, 1998). Since activation energy is highly temperature dependence, the NO_2 activation energy from Park et al. can be substituted into the present work because their temperatures (600-900℃) fall within the same range of interest as this experiment. By using the E_{NO2} from Park's work and coupling with Eq. 1.3 and Eq. 1.4, the A_{NO2} for the experiment in present study can be found. It is actually possible to use one condition of the initial and final NO_2 concentration at a particular temperature to find the pre-exponential factor. However, measurements are always prone to human and systematic errors. In order to avoid such bias, 10 measurements of NO_2 decomposition are used for the fitting. The fitted A_{NO2} is found to be 1.59 x 10^{-11} cm^3 $molecule^{-1}$ s^{-1}, which is a factor of 2 higher than Park's work but still within the expected range of uncertainty.

With this frequency factor, the NO_2 decomposition can be modeled as seen in Figure 1.7 while holding the volumetric flow rate constant. As expected, the NO_2 decomposition shows a more prominent decrease in mixing ratio as the furnace temperature is increased.

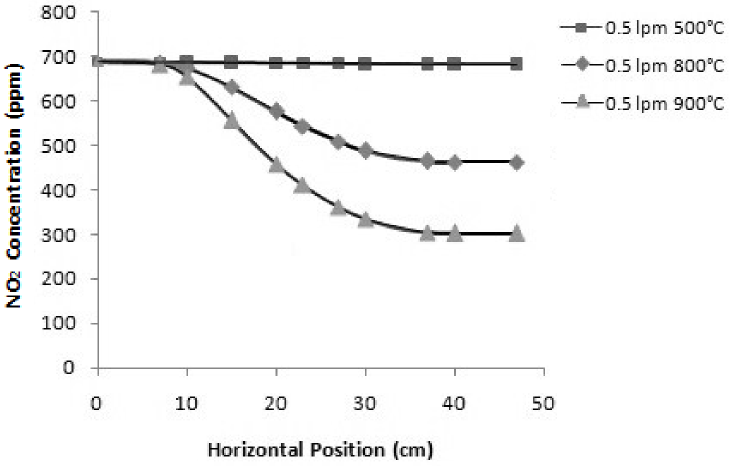

Figure 1.7 NO2 Concentration along the furnace

Figure 1.8 presents the measured vs. predicted NO_2 concentration (by the decomposition modeling) at the outlet under various initial NO_2 concentration. As can be seen the NO_2 decomposition modeling is quite precise with almost a 1 to 1 factor and high correlation.

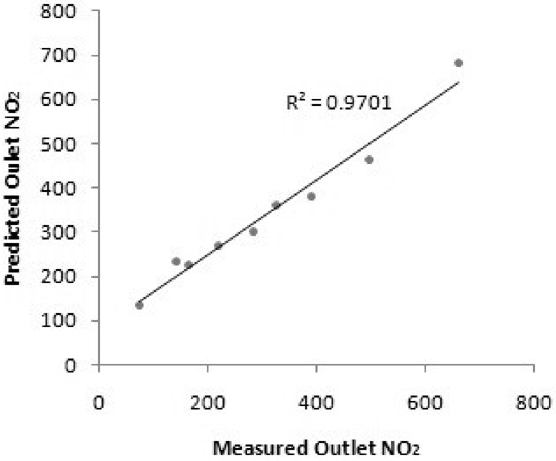

Figure 1.8 Predicted vs Measured NO2 concentration

1.3.3 Modeling the particle size decrease by oxidation

A nonlinear least-squares fitting is used on the experimental data of the shrinkage in particle size through the furnace by using the TDMA system. It has been proven that the decrease in peak particle diameter serves as a reliable parameter to derive the kinetics of soot oxidation (Shirvastava, 2009).

Higgins et al. (Higgins, 2002) has used an Arrhenius expression for parameters fitting to achieve the soot oxidation rate. However, NO_2 was not used during their study as an oxidant so the expression does not account for the NO_2 decomposition as mentioned in section 1.3.2. Therefore, for the current study, a modified form of the Arrhenius expression given in Eq. 1.5 is used to empirically describe the decrease in particle diameter for variable NO_2 concentration and non-uniform temperature within the furnace (Stanmore, 2001). The temperature is raise to the ½ to roughly account for the dependence of collision frequency on temperature (Higgins, 2002). The reaction order, n, with respect to NO_2 cannot be determined experimentally as soot is subjected to changing NO_2 concentration in the furnace due to decomposition. To be consistent with the reported reaction order from most studies, especially the ones that will be compared in section 1.5 to current work, n is assumed to be unity.

$$\mathbf{\dot{D_p} = -A_{soot}T^{1/2}\exp\left(-\frac{E_{soot}}{RT}\right)[NO_2]^n} \qquad \text{Eq. 1.5}$$

where $\dot{D_p}$ *is the rate of decrease of particle diameter with time,* A_{soot} *is the frequency factor,* E_{soot} *is the activation energy, R is the universal gas constant, n is the reaction order of the soot with respect to* NO_2*, T is the absolute furnace temperature in Kelvin,* NO_2 *is the concentration in molecules* cm^{-3} *at any given axial location within the furnace.*

The rate of decrease in particle size can be related to the total particle diameter shrinkage due to oxidation in the furnace by integrating the diameter change as the particles travels through the length of the reactor as in Eq. 1.6. The velocity profile that varies linearly with temperature along the tube length can be related to the volumetric flow rate and cross sectional area of the tube. This can be achieved by using the dependence of the rate and flow velocity on temperature as in Eq. 1.7.

$$\mathbf{\Delta D_p = \int_0^L \frac{\dot{D_p}(x)}{u(x)} dx} \qquad \text{Eq. 1.6}$$

where x is the horizontal position in the reactor tube, L is the length of the tube, and u(x) is the flow velocity along the tube length.

$$\mathbf{u(x) = \frac{4}{3} u_m \frac{T(x)}{T_0}} \qquad \text{Eq. 1.7}$$

where $\frac{4}{3}u_m$ *is the peak volumetric flow velocity assuming laminar flow, T(x) is the temperature at various axial location,* T_0 *is the inlet temperature.*

Thus, prediction of ΔD_p can be derived corresponding to the varying NO_2 mixing ratio and non-uniform furnace temperature using Eq. 1.5 and Eq. 1.6. The values of A_{soot} and E_{soot} are found from fitting the modeled ΔD_p to those found from experimental measurements.

1.4 Result

1.4.1 Prediction of particle diameter decrease ΔD_p

The A_{soot} and E_{soot} were found with least square fitting of 15 different values of measured ΔD_p within the 500-950°C furnace temperature range and various inlet NO_2 mixing ratios of 200-600 ppm. Through this fitting, it is found that the activation energy E_{soot} is 47.1 kJ mol^{-1} and pre-exponential factor A_{soot} is 2.4 x 10^{-14} nm K$^{-0.5}$ cm^3 molecule^{-1} s^{-1}. Figure 1.9 shows that the quality of the fit in predicting the measured decrease in particle size is very reasonable and good. Also soot oxidation rate (dD_p/dt) can be determined from the fitting and represented in Figure 1.10; the plot clearly shows that the instantaneous soot oxidation rate is a function of NO_2 mixing ratio and is the greatest at the axial center of the furnace where temperature is the highest.

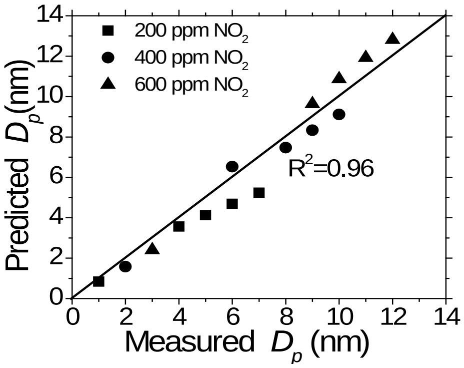

Figure 1.9 Comparison of measured and predicted ΔDp

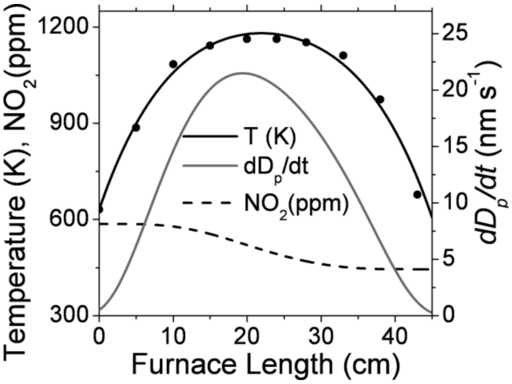

Figure 1.10 Variation of temperature, NO2 concentrations, and soot oxidation rates in the furnace

1.4.2 Oxidative and non-oxidative components of ΔD_p

Table 1.2 gives a more detail representation of the measured outlet particle diameter decrease at varying furnace temperatures and inlet NO_2 mixing ratios. An interesting observation made is that the particles at high furnace temperature show modest size reduction even when the soot is submerged in only N_2 environment with 0 ppm of NO_2. Nienow et al. had also come across this similar finding with the only difference being a smaller shrinkage in size due the shorter aerosol particles residence time inside the furnace (Nienow, 2005).

Set-point Temperature °C	(a) 0 ppm NO_2	(b) 200 ppm NO_2	(c) 400 ppm NO_2	(d) 600 ppm NO_2	(a-b) ΔD_p 200 ppm NO_2	(a-c) ΔD_p 400 ppm NO_2	(a-d) ΔD_p 600 ppm NO_2
500	40 nm	39 nm	38 nm	37 nm	1 nm	2 nm	3 nm
800	38 nm	34 nm	32 nm	29 nm	4 nm	6 nm	9 nm
850	36 nm	31 nm	28 nm	26 nm	5 nm	8 nm	10 nm
900	34 nm	28 nm	25 nm	23 nm	6 nm	9 nm	11 nm
950	32 nm	25 nm	22 nm	20 nm	7 nm	10 nm	12 nm

Table 1.2 Measured particle sizes and ΔDp values at varying inlet NO2 mixing ratios and temperatures

Since the particle is 40 nm, which has been seen in TEM image to fall in the range of spherical particles, densification is not possible; hence, the likelihood of size reduction from thermally induced restructuring of aggregates is very low. In this work, it is found that organic carbon contents of the diffusion flame contribute a significant amount (up to 40%) of the total carbon through conducting a thermal optical analysis of the soot collected on quartz filters. Volatile organic compounds have boiling point roughly in the range of 50-250°C. As a result, most of the semivolatile organics (SVOCs) cannot contribute to the soot oxidation under the experimental conditions in this study because they should have already evaporated due to the high furnace temperature of 500-950°C. Additionally, in conjunction with early stages dilution, the further dilution in DMA-1 decreases the mole fraction of SVOCs in the gaseous environment even more. With the assumption that the total partial pressure remains constant in the sampling line, more SVOCs continue to evaporate to re-achieve the equilibrium partial pressure. However, it is plausible for those strongly adsorbed relatively nonvolatile OC, such as PAHs, to be less prone to evaporate at lower end of the temperature range in this experiment (Muckenhuber, 2006). Also, the decomposition of the oxygen containing functional group at high furnace temperature can potentially be responsible for the size reduction observed under the N_2 environment without NO_2 as the oxidant (Muckenhuber, 2007).

Since this finding of the non-oxidative and oxidative parameters of ΔD_p contributes significantly to the derivation of oxidation kinetics, it is critical to separate them by assuming that these two components are additive as in Eq. 1.8 (Nienow, 2005).

$$\Delta \mathbf{D}_{\mathbf{p}}^{\mathbf{NO_2}} = \Delta \mathbf{D}_{\mathbf{p}} - \Delta \mathbf{D}_{\mathbf{p}}^{\mathbf{N_2}} \qquad \text{Eq. 1.8}$$

In other words, to avoid bias in the kinetics analysis, the oxidative component is found by subtracting ΔD_p under N_2 environment from the total ΔD_p due to both NO_2 and N_2 to achieve the last three columns of Table 1.2.

1.4.3 TDMA particle size distribution after the furnace

It is also beneficial to observe the particle number size distribution, dN/dlogD_p , from the TDMA scans by varying the furnace set point temperature and NO_2 mixing ratios as shown in Figure 1.11 and Figure 1.12, respectively. Both figures indicate that the particle size reduction is highly dependent on the increase in NO_2 concentration and furnace set point temperature. Even though a monodisperse line of the uniform 40 nm initial particles sizes is injected into the furnace, a broadened rather than narrowed particle size distribution due to oxidation is found at the outlet.

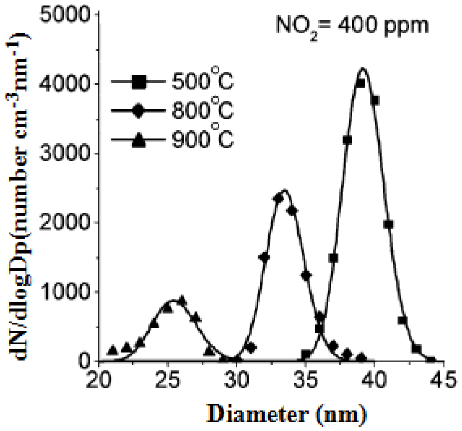

Figure 1.11 Size distribution from varying furnace temperature at a constant NO2 concentration of 400 ppm

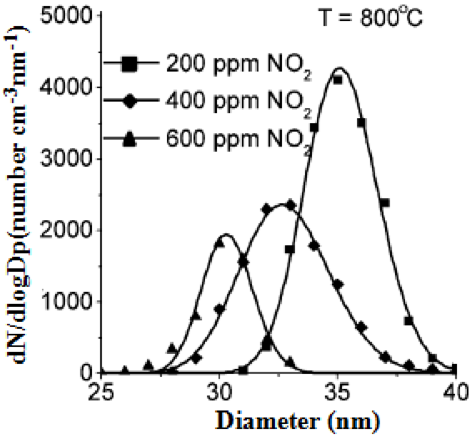

Figure 1.12 Size distribution from varying inlet NO2 concentrations at a constant furnace temperature of 800°C

This can be caused by the different residence times and oxidation duration that the particles experience within the reactor. There are several sources responsible for the varying residence time distribution among the soot particles:

1) The parabolic velocity profile inside the tube allows particles to have maximum velocity at the center and static, assuming no slip condition, at the wall.

2) The high furnace temperature causes buoyancy-induced temperatures effect (Shrivastava, 2009). Interruption in the flow due to buoyancy can potentially maneuver particles into complicated trajectory through the flow tube and can increase the residence time.

3) Thermophoresis contributes to motion of particles from high to low temperature region (Shirvastava, 2009). Also, the particles may move radially to some extent due to radial temperature distribution. Radial temperature distribution has not been accounted for in this study.

1.5 Discussion

1.5.1 Comparison with soot oxidation study: Case #1

Kamm et al. used nine quartz tubes, each containing quart wool plug loaded with soot generated from a spark generator, and were aligned in an oven thermostated between 200-350°C with 1000 ppm of NO_2 (Kamm, 2004). They were able to derive the activation energy for the soot to be 73 ± 6 kJ mol^{-1}, which is approximately 1.55 times higher than the E_{soot} reported in this current study. Kamm et al. lower experimental temperature range when compared to present work accounts partially for the differences in activation energy value since the oxidation rate is strongly dependent on temperatures. Kamm et al. reported nonlinearity in their Arrhenius plot implying a complex gasification mechanism with different rate-determining steps at different temperatures (Kamm, 2004). Another uncertainty that attributes significantly to the higher activation energy in Kamm et al. comes from using a 3-parameter fitting on only 4 experimental data points to model the temperature dependence for the soot oxidation. This insufficient and scarcity of data points can cause major bias during the derivation of the activation energy. Nonetheless, similar to our study, Kamm et al. also suggested the gasification rate of soot to be indeed first order in NO_2; however, Kamm et al. arrived at such conclusion through observing the plots of the characteristic time constant and various NO_2 mixing ratio while holding the temperature constant (Kamm, 2004).

1.5.2 Comparison with soot oxidation study: Case #2

Similar to the current study, Choo et al. also used an HTO-TDMA experimental set up to analyze soot oxidation with the influence of NO_2 in the temperature range of

200-700°C (Choo, 2008). There results also show that as the reactor temperature and NO_2 concentration increase, the geometric mean diameter (GMD) decrease ratio increases as seen in Table 1.3. Another similar finding to present study is that the GMD of the carbon nanoparticles decrease slightly at 0 ppm of NO_2. However, they did not consider separating the non-oxidative and oxidative components of ΔD_p as in section 1.4.2.

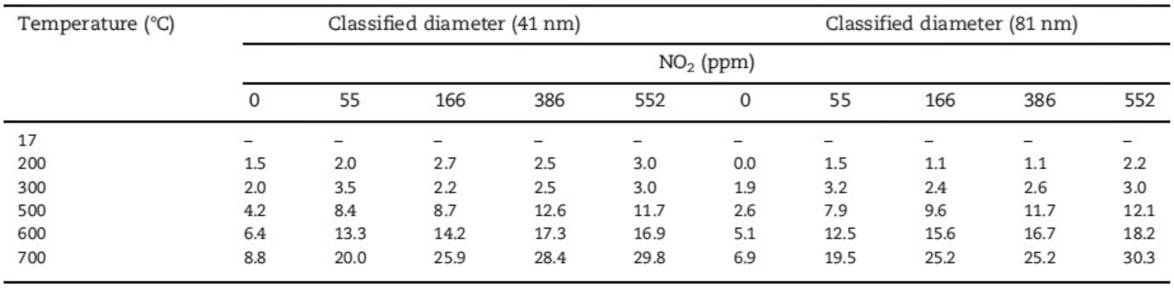

Temperature (°C)	Classified diameter (41 nm)					Classified diameter (81 nm)				
	NO_2 (ppm)									
	0	55	166	386	552	0	55	166	386	552
17	–	–	–	–	–	–	–	–	–	–
200	1.5	2.0	2.7	2.5	3.0	0.0	1.5	1.1	1.1	2.2
300	2.0	3.5	2.2	2.5	3.0	1.9	3.2	2.4	2.6	3.0
500	4.2	8.4	8.7	12.6	11.7	2.6	7.9	9.6	11.7	12.1
600	6.4	13.3	14.2	17.3	16.9	5.1	12.5	15.6	16.7	18.2
700	8.8	20.0	25.9	28.4	29.8	6.9	19.5	25.2	25.2	30.3

Table 1.3 GMD decrease ratio (%) of carbon nanoparticles with various temperatures and NO2 concentrations for classified particle diameters of 41 nm and 81 nm

Choo et al. applied Eq. 1.9 and Eq. 1.10 to generate a log(k) vs. 1/T Arrhenius plot to get a proportional relation between the slope and activation energy. This is an incorrect approach to achieve the soot activation energy since it does not account for NO_2 decomposition and non-uniform temperature profile along the furnace.

$$\mathbf{k} = \frac{\mathbf{m_{in} - m_{out}}}{\mathbf{A_s dt}} \qquad \text{Eq. 1.9}$$

where m_{in} *and* m_{out} *are the mass at the inlet and outlet of furnace, respectively,* A_s *is the surface area assuming spherical morphology, and dt is the reactor residence time.*

$$\mathbf{k = Ae^{-E_a/RT}} \qquad \text{Eq. 1.10}$$

where A is the frequency factor, E_a *is the activation energy, R is the universal gas constant, and T is the mean temperature within the furnace.*

Thus, in order to make appropriate comparison with current study, it is necessary to reanalyze Choo et al. oxidation data. In the re-analysis procedure, the E_{soot} is recomputed with accounting for: 1) the temperature distribution at 500, 600 and 700°C provided in Figure 4 of Choo et al. study 2) the NO_2 decomposition analysis along Choo's furnace at mixing ratios of 166, 386, 552 ppm and 3) the correction for non-oxidative components of ΔD_p. A two parameter least square fitting with assuming the reaction order to be unity like section 1.3.3 is generated for Choo et al. nine data points. With this re-analysis, the new E_{soot} value is found to be 45.7 kJ mol^{-1}. This is significantly lower than Choo et al. former reported value but corresponds highly to the activation energy (47.1 kJ mol^{-1}) found in section 1.4.1 of this study. With the reanalyzed E_{soot} and A_{soot}, the NO_2 mixing ratios are computed to decrease up to 27% when furnace temperature is at 700°C. Therefore, this shows that the omission of NO_2 decomposition and errors in data analysis as mentioned in this section for Choo et al. measurements are heavily responsible for the overestimation of the E_{soot} by a factor of 1.7 when compared to current study.

1.5.3 Comparison with soot oxidation study: Case #3

To elucidate the characteristics of soot oxidation, the commercial carbon black (Printex-U) was used as a model soot for its oxidation consistency characteristics in Lee et al. study. The kinetics constants were derived by a flow reactor that simulates the condition of a diesel particulate filter and diesel exhaust gas. They found that the activation energy for oxidation with NO_2-O_2 environment to be 60 ± 3 kJ mol^{-1}. The E_{soot} is slightly lower than current study because the temperature examined in Lee's study is

250-500°C instead of the higher temperature range in our study of 500-950°C. This temperature range is representative of the temperature during the expansion stroke of diesel engine and at the high temperature end for DPF (Ma, 2008).

1.5.4 Comparison of soot oxidation rate in the presence of air and NO_2

Consistent with many former studies, this current work has reported much lower activation energy for soot oxidation with NO_2 as compared to air or O_2. The activation energy for soot oxidation in the presence of O_2 has been derived to be in the range of 164-177 kJ mol^{-1} (Higgins, 2002; Lee, 2007) whereas with NO_2 from current study is 47.1 kJ mol^{-1}. This shows that NO_2 is a very effective oxidant since its contribution is significant in reducing the chemical reaction barrier for oxidation to take place.

Higgins has reported that despite the 3 initial particles (40, 93, 130 nm) in their study experience the same activation energy, the oxidation rates are not the same due to the differences in morphology, density and composition of the particles. This makes it impossible to fit the different initial particle sizes with a single frequency factor. Thus, it is essential to investigate the surface oxidation rates through the derivation from the particle size decrease rate $\dot{D}_p$ from section 1.3.3. By modeling soot as spheres with constant density of 1800 kg m^{-3}, the surface oxidation rate from diameter decrease rate can be computed from taking the derivative of Eq. 1.11 to achieve Eq. 1.12 (Higgins, 2002).

$$\frac{\mathbf{dm_s}}{\mathbf{dt}} = -\dot{\mathbf{w}}\mathbf{A_s} \qquad \text{Eq. 1.11}$$

where A_s *is the soot surface area,* m_s *is the particle mass,* $\dot{w}$ *is the surface oxidation rate*

$$\dot{\mathbf{w}} = \frac{\boldsymbol{\rho}_{\mathbf{s}}(\mathbf{D}_{\mathbf{p,i}}-\mathbf{D}_{\mathbf{p,f}})}{\mathbf{2\tau}} = \frac{\boldsymbol{\rho}_{\mathbf{s}}}{\mathbf{2}}\dot{\mathbf{D}}_{\mathbf{p}} \qquad \text{Eq. 1.12}$$

where $D_{p,i}$ *and* $D_{p,f}$ *are the initial and final mobility diameter of the soot particle,* ρ_s *is the soot density,* τ *is the residence time, and* $\dot{D}_p$ *is the particle diameter rate of change.*

Fig 1.13 gives a comparison between the surface oxidation rates of soot in the presence of various NO_2 mixing ratios with that in an air environment that has been derived by Higgins et al. From former soot studies (Ehrburger, 2002), it has been established that NO_2 is a much stronger oxidant than air and O_2 at the low temperature range (T ≤ 500°C). But, interestingly, even at higher temperature region (800-900°C) as seen in Figure 1.13, the surface specific oxidation rate with NO_2 still reveals to be within comparable ranges with the oxidation rate that is only in air environment. Therefore, a critical conclusion that can be withdrawn is that even a small level in parts per million of NO_2 is already sufficient enough to generate a similar oxidation effects as the atmospherically abundant amount of O_2 (20% mixing ratio of O_2 in air). Hence, this proves once again NO_2 to be a stronger oxidant than O_2.

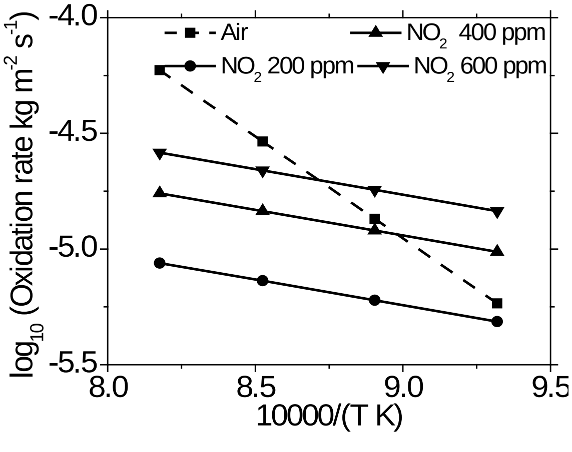

Figure 1.13 Comparison of soot oxidation rate in the present study vs. soot oxidation by air in Higgins et al.

1.6 Conclusion

In this study, the oxidation kinetics are investigated on soot generated from a diffusion flame using ethylene as the fuel and measurements are made with the HTO-TDMA system under various NO_2 mixing ratios (0-600ppm) within a flow reactor in the temperature range from 500 to 950℃. It embraces many advantages over former studies such as accounting for the non-uniform temperature distribution within the reactor and NO_2 decomposition at high temperatures. The experimental condition is conducted at the high temperature range because the oxidation shows insignificant particle size changes due to instruments' limitation under low temperature. With the assumption that the soot oxidation with NO_2 have a reaction order of unity, it is calculated that the pre-exponential factor is 2.4×10^{-14} nm $K^{-0.5}$ s^{-1} cm^3 $molecule^{-1}$ and the activation energy E_{soot} is 47.1 kJ mol^{-1}. The activation energy has shown to be in good agreement with the reanalyzed data from Choo et al (Choo, 2008) and has minor differences with other studies (Kamm, 2004; Lee, 2007) because these studies are conducted at a slightly lower temperature than this current work. This work also provide proofs indicating NO_2 being a stronger and more relevant oxidant than O_2. The kinetics of soot oxidation from this research is valuable for applications at high temperature range like inside engine cylinder, flame condition or the high temperature end of diesel exhaust.

It would be very beneficial for future studies to obtain kinetics data for lower temperature range by using this HTO-TDMA experimental method but with instruments that have higher resolution. Also, the investigation of soot oxidation rates with the presence of other oxidants, such as O_2 and H_2O, is definitely of interest. Furthermore, testing the postulation that NO_2 and O_2 can synergistically make oxidation more efficient is a critical possible subject of further studies. Research should also be directed toward analyzing soot that is generated by different kind of fuels and a real world source. Nonetheless, with the growing emphasis on reducing diesel particulate emission, the information on the diesel soot burnout through oxidation from this research is definitely very beneficial. It will help in improving the design parameters such that the emission control technologies for in-cylinder, after treatment system (DPF for on-road diesel) and regeneration process to become even more smooth and effective.

Chapter 2 Interpretation of secondary organic aerosol formation from diesel exhausts photo-oxidation in an environmental chamber

2.1 Introduction

2.1.1 Background

Gaseous primary organic aerosols (POA), which are directly emitted from anthropogenic sources, are oxidized in the atmosphere to form semi-volatile products (SVOC and IVOC) and set the foundation for the formation of secondary organic aerosol (SOA) due to their low volatility. SOA formation in the atmosphere can be perceived as a three step process. 1) the gas-phase photochemical oxidation that transform the parent volatile organic compounds (VOC) into SOA products 2) the competition between gas and particle phase partitioning of SOA compounds, 3) particulate-phase reactions that can convert the SOA species to other chemical compounds (Seinfield, 2006). Former study has shown that an estimated amount of 70% of organic aerosols is secondary in nature (Hallquist, 2009). Organic aerosol (OA) contributes approximately 20-90% of aerosol mass in the lower troposphere (Kanakidou, 2005). Since OA plays a major role in escalating the acute and chronic, adverse health effects reported by many studies (EPA, 2002; Oberdurster, 2000; Pope,2006; Davidson, 2005) and global climate changes (Kanakidou, 2005; IPCC, 2007), emission regulations have become very stringent and demand lower diesel emission technologies.

Accelerating the gas-phase chemistry by submerging the particulates in a high temperature and strong sunlight intensity can tremendously increase the rate of SOA formation. Changes in oxidant levels, precursor concentrations, temperature and relative humidity can lead to many different product distributions as well. Hence, similar to many SOA former studies, current work is also done inside an environmental chamber to simulate as near to atmospheric conditions as possible. In general, SOA yields increase as additional amounts of parent VOCs react in the same air parcel and in cases containing significant amount of preexisting organic aerosol (Strader, 1999).

2.1.2 SOA from diesel exhaust

Although there are many sources of POA and SOA formation, diesel engine draws immense interest. Figure 2.1 shows a depiction of diesel particles' structure which contains mainly fractal-like agglomerates of elemental carbon, volatile organic, ashes, and sulfur-containing compounds that are condensed onto the surface.

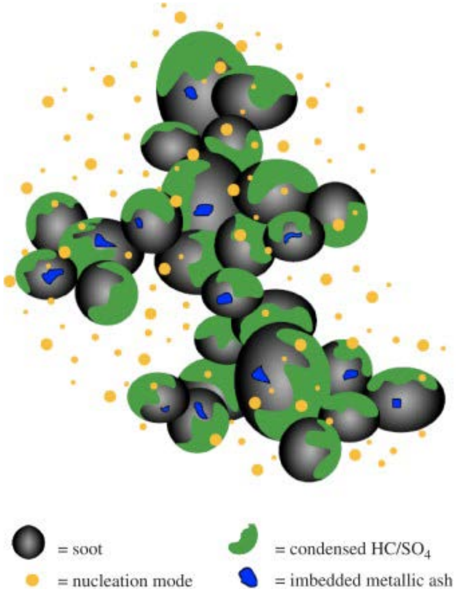

Figure 2.1 Conception of diesel particulate matter (Maricq, 2007)

Beside diesel being a major source of urban POA (Schauer, 1996), it has also been reported that the rate of SOA formation due to photo-oxidation from diesel exhaust is extremely rapid and high (Robinson, 2007). Diesel engines are widely used to power heavy duty transportation vehicles due to their high thermal efficiencies. Unfortunately, diesel engine exhaust, as expected, has been a great subject of concern to researchers, engine manufacturers, and regulatory agencies since it has been discovered to be one of the major sources of atmospheric pollution, especially in term of particulate matter and NO_2.

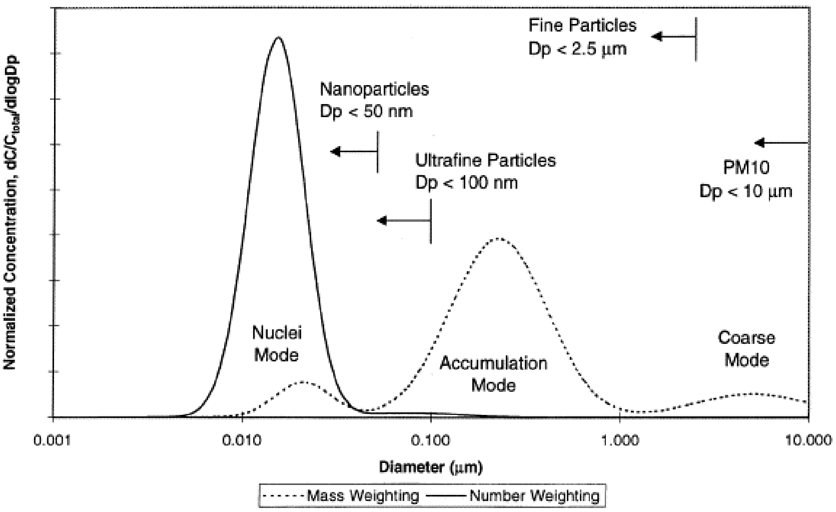

Figure 2.2 Diesel particulate tri-modal size distribution

A typical lognormal, tri-modal particle size distribution of diesel particulates is categorized into three distinctive groups that are named as nucleation, accumulation and coarse mode as shown in Figure 2.2. The VOC and sulfur contents of the nucleation mode particles are produced during the dilution and cooling process in the diesel exhaust. The sizes of these particulates fall below 30 nm. They are strongly influenced by after-treatment systems and related nonlinearly with temperature and dilution ratio (Lahde, 2009). The nucleation mode particles contribute approximately up to 20% of particle mass and more than 90% of particle number concentration (Kittelson, 1998). The accumulation mode, with diameter extending from 0.1-2.5 µm, accounts for most of the aerosol surface area and a substantial part of the mass (10-15% of particle number and more than 80% of particle mass in total diesel emission). Due to experiencing weak removal mechanisms by rainout or washout, these particles are able to accumulate through the coagulation of nuclei mode particles and vapor condensation of volatile hydrocarbons to grow in size. When the coagulations occur more frequently and rapidly, the particles reach the coarse particle regime. Coarse mode particles are re-entrained agglomerates that have sufficiently large sedimentation velocities so their lifetime in the atmosphere is reasonably short (a few hours or days). Since removal mechanisms are only efficient at the small and large particle extremes of the size spectrum, accumulation mode particles tend to have a longer atmospheric residence times than those in either the nuclei or course mode.

2.1.3 Objective

Many important findings with regard to photo-oxidation of aromatic hydrocarbon have been found through a number of studies (Arey, 2009; Calvert, 2002; Johnson, 2004; Olariu, 2002, Takekawa; 2003, Volkamer, 2002). It was recognized that the first generational products of aromatic compounds photo-oxidation only account for at most 50% of the carbon balance, which leaves the other half of the products in aromatics photo-oxidation as unidentified (Calvert, 2002). These first generation products can further form an additional wide array of compounds through reacting with OH, O_3 and/or NO_3. Additionally, NO_x affects significantly on the fraction of VOC that reacts with OH, O_3 and NO_3.

SOA formation is governed by a complex series of reactions of a large number of organic species (Kroll, 2008). Although many products from these reactions have been observed, their relative importance toward SOA formation is still very speculative. Also, studies on SOA formation due to first generational aromatic compounds are still scarce. There have been numerous attempts to model SOA production based on gas-phase reaction mechanisms of aromatics incorporating gas-to-particle partitioning. Unfortunately, the developed models are within reasonable agreements with data/measurements under only limited experimental conditions or when parameters such as partitioning coefficients were arbitrarily adjusted (Cai, 2008; Cao, 2010; Johnson, 2005). Also, established air quality models of organic aerosol evolution inside the environmental chambers have been shown to under-predict the real atmospheric reaction (Volkamer, 2006), pointing toward missing knowledge regarding precursors and physical/chemical processes that govern the formation and evolution of the aerosol in the atmosphere. For instance, the two product model of Odum et al. is expected to be relatively accurate for the experimental conditions used for its derivation (Odum, 1997). However, there are still major limitations in the model under significantly different scenarios from their laboratory conditions. Under those situations, the model predictions have a significant uncertainty factor ≥ 2 due to simplistic assumption about environmental conditions. Hence, one of the objectives of this study is to investigate the chemical aging of the particulates from the diesel exhaust inside an environmental chamber. This allows an improve understanding of complex multi-generational aromatic reactions leading to SOA formation since the measurements are made within an environment that simulates as close as possible to real-world atmospheric conditions.

Former studies (Robinson, 2007; Grieshop, 2009) have observed significant effects of diesel engine on SOA but other studies (Samy, 2010; Chirico, 2010) have reported weak relation between SOA formation and diesel exhaust without the addition of radical sources or additional hydrocarbon. Therefore, due to these uncertainties from previous studies, further investigation is required to better understand the SOA formation process and causes of discrepancy between these studies. Many studies (Chirico, 2007; Samy, 2010) have computed the mass of SOA based on the wall-loss-corrected particle volume concentration and by assuming spherical particles. However, in the accumulation mode, diesel particles contain mainly fractal like agglomerates. Indeed due to these void spaces, it is reported that the effective density decreases as the particle size increases (Park, 2003). However, SOA coating can fill in the voids of these fractal-like diesel particles and increases the density. Nonetheless, the assumption of spherical shaped particles is not true for either situation. Therefore, another focus of this study is investigating the changes in diesel agglomerates' effective density inside an environmental chamber during the gas-to-particle partitioning of SOA.

Furthermore, since no investigation has been made prior to study on the effect of dilution methods on SOA formation, this is another objective of current work. More specifically, this is the first research effort that has been done to identify the impact of different dilution techniques (rapid or stagnant) and environmental chamber filling methods on the evolution of diesel particles' effective density.

2.2 Experimental Method

2.2.1 Mezzanine chamber

The experiment is conducted inside the mezzanine chamber, which is located at CE-CERT/UCR, Riverside. It is a 2.5 m x 3 m x 7.8 m enclosure where a 12 m^3 2 mil (54 μm) FEP Teflon® film reactor is installed as shown in Figure 2.3. This enclosure is covered with reflective aluminum sheeting and is illuminated with 170 of 40W black lights with peak intensity at 350 nm (SYLVANIA, 350 BL) generating the NO_2 photolysis rate of 0.6 min^{-1}. In order to ensure the air inside the enclosure does not get overheated, 6 fans are installed as shown in Figure 2.3 to thoroughly mix the air inside the Teflon reactor with controlled room temperature air. The enclosure temperature is typically maintained approximately at 25-28°C. Also to minimize heating in the enclosure, there is a minimum of 1m space between the reactor surface and black lights even when the bag is full. Before every experiment, the bag is flushed several times/ overnight with purified air (Aadco 737 series air purification system (Cleves, Ohio)) until the background particle concentration is below the limit of detection (<0.2 cm^3).

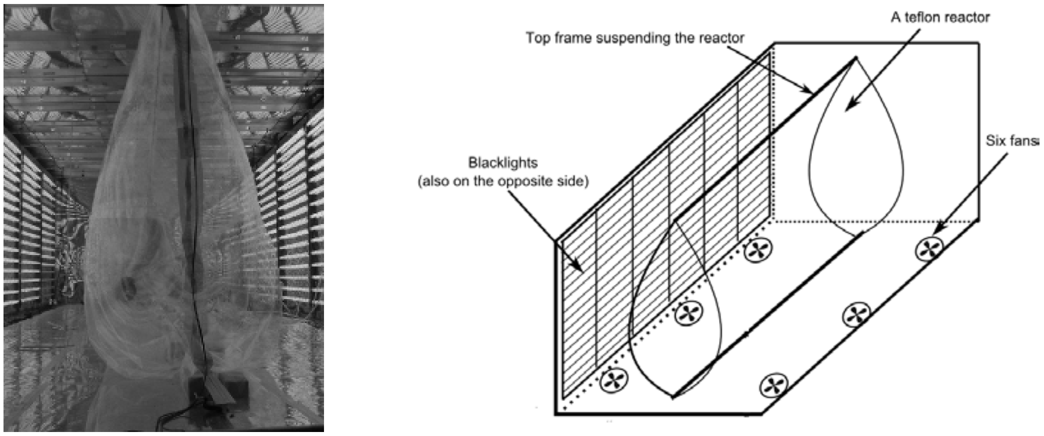

Figure 2.3 Schematic diagram of CE-CERT mezzanine chamber facility

2.2.2 Analytical Instruments used for gas/particle analysis

APM-SMPS:

A custom built Scanning Mobility Particle Sizer (SMPS) is used to monitor the size between 28 nm to 700 nm. The method of SMPS is based on the principle of relating particle electrical mobility to particle size such that no size calibration is necessary. In the SMPS measurement the concentration are measured directly without assuming the shape of the particle size distribution. The aerosol particle mass analyzer (APM, Kanomax) is also used in this experiment to enable mass selection by balancing the centrifugal and electrostatic forces on particles passing through a small annular gap between two cylinders that are rotating at a set angular momentum. This allows the APM to classify the particles independent of the particle size, shape and orientation. The APM takes advantage of the classification method of mass-to-charge ratio to measure a single aerosol particle. For the APM system, 0.01-100 fg is approximately equivalent to 30-580 nm particles with the unit density assumption (Kanomax Japan, Inc.).

The particle effective density is directly determined by using the APM in series with the SMPS. Traditionally, the DMA-APM had been used in many former studies (McMurry, 2002; Xue, 2009); the DMA has been placed ahead of the APM to first select aerosol base on electrical mobility followed by the APM to classify the size distribution base on mass. However, with the aerosol diameter changing rapidly in chamber experiments, the DMA-APM setup suffers from the slow APM response due to the long settling times when the voltage is changed through stepping mode. Additionally, this setup encounters the frequent problem of low signal to noise ratio due to the narrow transfer function of the DMA (Malloy, 2009). As a result, this current work uses the orientation of locating the APM in the upstream of the SMPS as seen in Figure 2.4. This allows the time resolution of the APM-SMPS to be improved by approximately 1 minute (Malloy, 2009) due to the rapid scanning characteristic of SMPS. The mass of the particle transmitted through the APM-SMPS is estimated by utilizing an independent SMPS that identifies the mode particle diameter and the initial assumed density. This estimated mass reduces the sampling time by setting the appropriate APM angular rotational speed and voltage that correspond with the narrow SMPS scan range. With the mass selected by the APM and the peak diameter from the SMPS located downstream of the APM, the density can be computed from Eq. 2.1. It is worth mentioning that ρ_e is equal to the true particle density if the aerosol is spherical; otherwise, it is the mobility effective density.

$$\boldsymbol{\rho_e = \frac{m_p}{\frac{\pi}{6} d_m^3}} \qquad \text{Eq. 2.1}$$

m_p is the mass of the particle, d_m is the mobility diameter

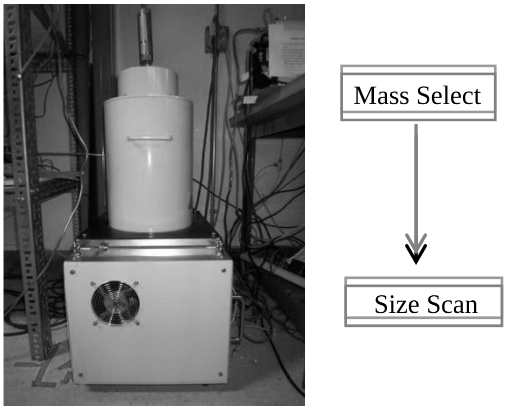

Figure 2.4 Aerosol particle mass analyzer-scanning mobility particle sizer

VTDMA:

The volatility tandem differential mobility analyzer (VTDMA) in Figure 2.5 Volatility Tandem Differential Mobility Analyzer is used to monitor the particle volatility.

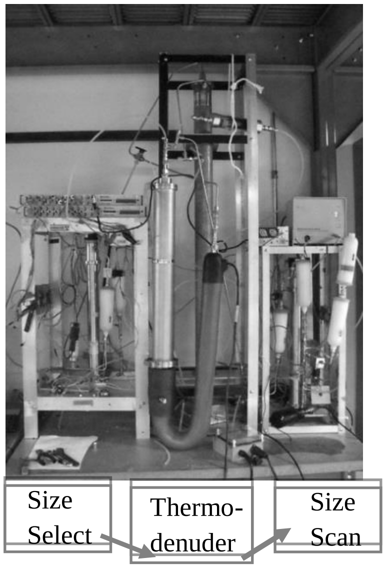

Figure 2.5 Volatility Tandem Differential Mobility Analyzer

Monodisperse aerosol that is selected in the first DMA with a known mobility diameter D_{mi} will get passed through a Dekati® thermodenuder (TD, residence time: approximately 17 seconds, temperature 100°C). VOCs and SVOCs are vaporized by high temperature through the aerosol heater in the TD. After the heating section, the compounds are adsorbed in an easily exchangeable active charcoal in which the sampling lines are cooled. These remaining particles that have survived from the high temperature oxidation are transported into the second SMPS to output the size distribution and concentration. This is done in order to address the volatile/non-volatile fractions at respective temperature by comparing the number density prior and after heating. The VTDMA is calibrated for each diameter setting using VFR of dry $(NH_4)_2SO_4$ seed aerosol and/or diesel particles at room temperature. The volume fraction remaining (VFR) is computed by Eq. 2.2.

$$\mathbf{VFR} = \left[\frac{\mathbf{D_{mf}}}{\mathbf{D_{mi}}}\right]^{\mathbf{3}} \qquad \text{Eq. 2.2}$$

where the D_{mi} *and* D_{mf} *is the mobility diameter before and after the TD, respectively.*

HR-ToF-AMS:

The high-resolution time-of-flight aerosol mass spectrometer (HR-ToF-AMS) is used to observe the chemical evolution of organic particulates. The operation mode of the HR-ToF-AMS can be alternated between the aerosol mass spectrum (AMS) and the particle time-of-flight (PToF). For this study only the AMS mode data is applied. A major role in this work is to predict the aerosol concentration base on the atmospheric climate and air impact. Even when the model outputs an accurate mass concentration but if the compositions of the SOA products are wrong, the model is still inefficient since it is achieving the right mass concentration for the wrong reasons. In other words, the model needs as many constraints as possible especially for the chemical composition.

The AMS is capable of providing the online quantitative data on the mass concentration, size distribution and atomic ratio of fine particulate components. This mode basic operation principle is to focus the particles into a tightly collimated beam onto a porous tungsten surface that is typically at 600-700°C. Under this temperature range and ultra-high vacuum, the non-refractory components of the particle are flash vaporized. The gaseous particles are then ionized using the 70 eV electron impact (EI) ionization. The resulting ions are then analyzed using a quadrouple mass spectrometer with unit mass-to-charge (m/z) resolution (Jayne, 2000). A mechanical chopper as seen in Figure 2.6 is used in the detection region to block the beam of signals that contain background gases. This background spectrum is subtracted from the MS to give a more accurate representation of the NR components of the sampled particles. During atmospheric sampling, gas phase species account for most of the signal at certain m/z peaks, with only additional peaks due to fragments, isotopes and doubly charged ions (Jayne, 2000).

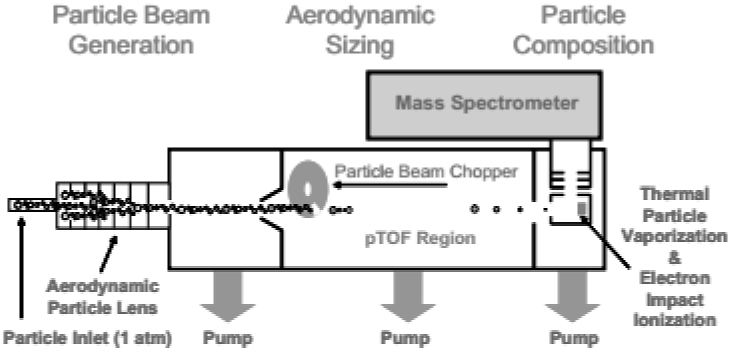

Figure 2.6 High Resolution Time-of-Flight Aerosol Mass Spectrometer

Although the AMS’s particle collection efficiency is low for particles <70 nm, this does not affect the current study. The geometric mean diameter of the diesel exhaust particles in this experiment grows to become above 70 nm due to coagulation and/or preferential wall loss of small particles. The instrument is used to obtain the high resolution mass spectrum of bulk aerosol that can be further applied for elemental analysis (C,H,N,O) (Aiken, 2008). With this information, it is possible to get the critical O/C and H/C ratios such that the $C_xH_yO_z$ formula unit can be determined.

Gas Analyzers:

The Teledyne analyzers 200E, 300E, and 400E models are used to measure the NO_x, CO, and O_3 concentration, respectively. A flame ionization detector (GC-FID, Agilent technology 6890) is used to measure ethene concentration. The FID passes the gas phase output from the GC column into a hydrogen flame so that the organic molecules get oxidized and ions can be generated. Hence, the number of ions is proportional to the concentration of the organic species in the gaseous stream. The collected ions produce an electrical signal which is then measured.

A summary of the analytical instruments used for gas as well as particle analysis are listed in Table 2.1.

Gas analysis		Targets	Note
GC-FID	Agilent 6890 Gas Chromatography - Flame Ionization Detector	Volatile Organic Compounds (VOCs)	Reactants and some products are quantified.
Gas analyzers (NOx, O_3, CO)			
Particle analysis		Targets	Note
SMPS	Scanning Mobility Particle Sizer	particle volume concentration, size-distribution	Particle volume concentration in combination with reacted hydrocarbon (ΔHC) is used to calculate SOA yield (PM mass/ ΔHC)
HR-ToF-AMS	Aerodyne High Resolution Time of Flight Aerosol Mass Spectrometer	on-line bulk chemical analysis	High resolution mass spectrum is analyzed to obtain bulk elemental composition of SOA (Aiken et al. 2008)
APM-SMPS	Kanomax Aerosol Particle Mass Analyzer - SMPS	density evolution	Particle mass slected by APM and particle diameter determined by SMPS is used to calculate effective density
VTDMA	Volatility Tandem Differential Mobility Analyzer	volatility evolution	Volume fraction remaining (VFR) after passing through 100 °C thermodenuder is used as an indication of particle volatility

Table 2.1 Analytical instruments used in the experiment

2.2.3 Dilution methods

The Pramac 3.6 kW generator (Yanmar Engine, E3750 MYHDI) that operates on ULSD fuel (sulfur content is less than 15ppm) is used for the diesel exhaust emission, which is similar to the type of engine used in other study (Robinson, 2007). In order to ensure the diesel exhaust have reached steady state, the engine is warmed up for 45 minutes prior to injection into the environmental chamber. This engine runs at 50% (medium load), 30% (low) load, and idling by controlling the resistive load bank (Swift-E STD, Simplex Inc.) that is connected to the engine.

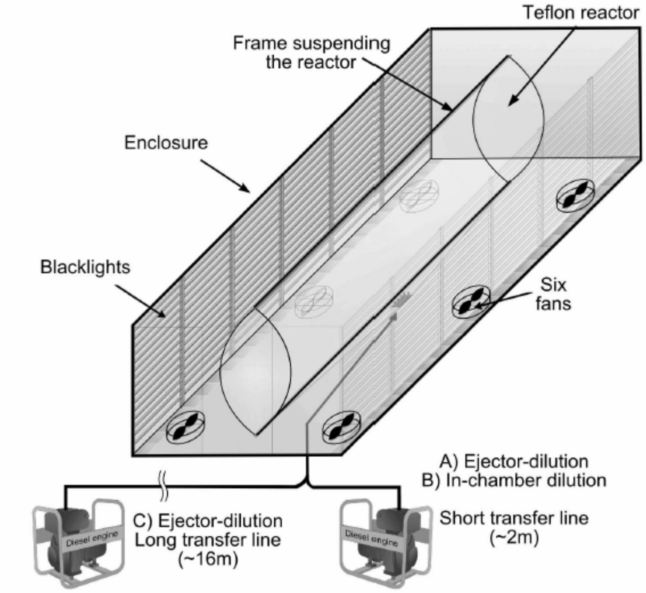

Figure 2.7 Various dilution methods for injection into the environmental chamber

The dilution of diesel exhaust is done by either an 1) ejector dilution system or 2) in-chamber dilution. For the first type, a custom built double ejector, two stages, variable residence time, micro-dilution tunnel similar that in Khalek et al. has been selected for current experimental apparatus (Khalek, 2000). By the time the aerosol flow reaches the secondary stage dilution, it reaches a high enough dilution ratio and speed such that there is only slow coagulation, and hence, nucleation is terminated. The ejector dilutor involves intensive mixing between the exhaust concentrations with compressed air. After the ejector dilutor, the sampling line will pass through either a 2 m or 16 m transfer line as shown in Figure 2.7 a) into an empty environmental chamber. On the other hand, Figure 2.7 b) depicts the other dilution method involving the transfer of undiluted exhaust from the 2 m short transfer line into the chamber for dilution. As oppose to the other rapid dilution case, this one involves a slow mixing process between the injected raw exhaust with the clean air inside the chamber.

2.3 Analysis of results from analytical instruments

Table 2.2 provide a summary of the initial particle volume/number concentration, initial NO_x, initial ethane, calculated OH concentration, fractal-like dimension, bulk effective density of the particles, and dilution ratio under the different experimental runs and engine load conditions.

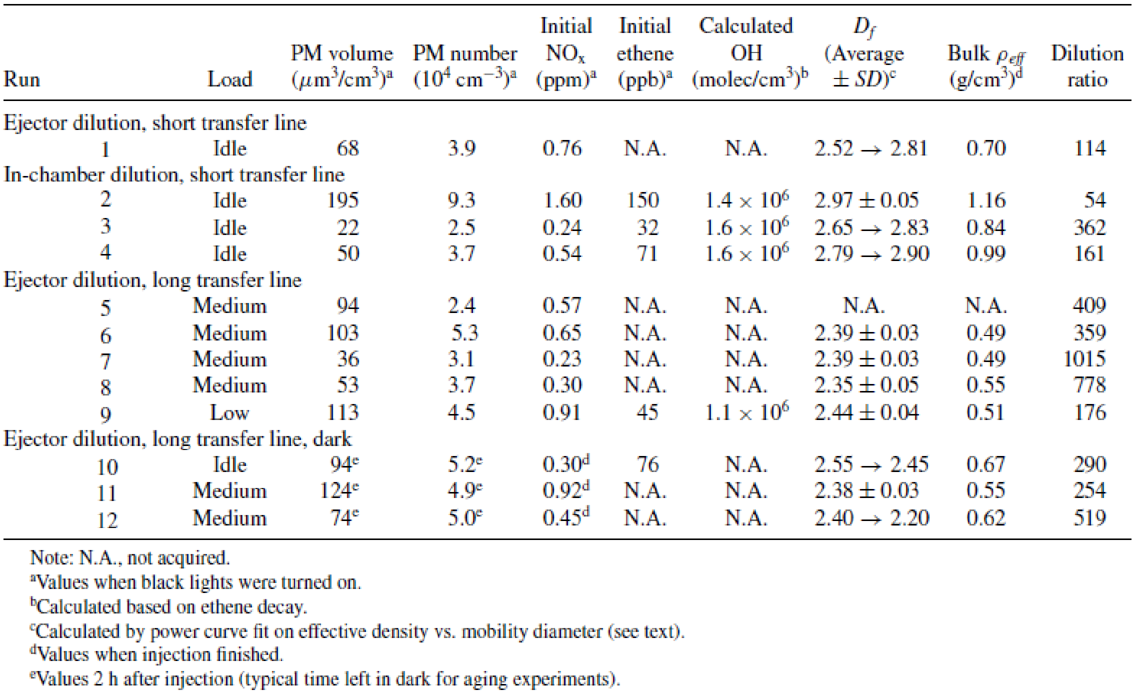

Run	Load	PM volume ($\mu m^3/cm^3$)^a	PM number (10^4 cm^{-3})^a	Initial NO_x (ppm)^a	Initial ethene (ppb)^a	Calculated OH (molec/cm^3)^b	D_f (Average ± *SD*)^c	Bulk ρ_{eff} (g/cm^3)^d	Dilution ratio
Ejector dilution, short transfer line									
1	Idle	68	3.9	0.76	N.A.	N.A.	2.52 → 2.81	0.70	114
In-chamber dilution, short transfer line									
2	Idle	195	9.3	1.60	150	1.4×10^6	2.97 ± 0.05	1.16	54
3	Idle	22	2.5	0.24	32	1.6×10^6	2.65 → 2.83	0.84	362
4	Idle	50	3.7	0.54	71	1.6×10^6	2.79 → 2.90	0.99	161
Ejector dilution, long transfer line									
5	Medium	94	2.4	0.57	N.A.	N.A.	N.A.	N.A.	409
6	Medium	103	5.3	0.65	N.A.	N.A.	2.39 ± 0.03	0.49	359
7	Medium	36	3.1	0.23	N.A.	N.A.	2.39 ± 0.03	0.49	1015
8	Medium	53	3.7	0.30	N.A.	N.A.	2.35 ± 0.05	0.55	778
9	Low	113	4.5	0.91	45	1.1×10^6	2.44 ± 0.04	0.51	176
Ejector dilution, long transfer line, dark									
10	Idle	94^e	5.2^e	0.30^d	76	N.A.	2.55 → 2.45	0.67	290
11	Medium	124^e	4.9^e	0.92^d	N.A.	N.A.	2.38 ± 0.03	0.55	254
12	Medium	74^e	5.0^e	0.45^d	N.A.	N.A.	2.40 → 2.20	0.62	519

Note: N.A., not acquired.

[a] Values when black lights were turned on.

[b] Calculated based on ethene decay.

[c] Calculated by power curve fit on effective density vs. mobility diameter (see text).

[d] Values when injection finished.

[e] Values 2 h after injection (typical time left in dark for aging experiments).

Table 2.2 Engine load, initial concentrations, calculated OH concentration, Df, bulk effective density, and overall dilution

The dilution ratio is found by taking the ratio of NO_x concentration in the raw exhaust to the measured value inside the environmental chamber. To obtain the effective densities, the APM-SMPS is programmed to select 3-5 different particle masses in approximately 20 minutes to obtain the particle density as a function of particle mass. By fitting these effective measured densities and particles' mobility size diameter into the power equation relationship (Eq. 2.3) as suggested by Park et al. (Park, 2003), the fractal-like dimension can be obtained. This power function can then be used to interpolate and extrapolate particle density within the size range of the SMPS measurement. By integrating particle volume and bulk effective density distribution, the particle mass concentration can be computed as a function of mobility diameter.

$$\boldsymbol{\rho_{eff} = Cd_m^{D_f-3}} \qquad \text{Eq. 2.3}$$

As seen from run 1 of Table 2.2 in Figure 2.8, the fractal dimension increases after turning on black lights from 2.52 to 2.81±0.06, suggesting SOA condensation possibility.

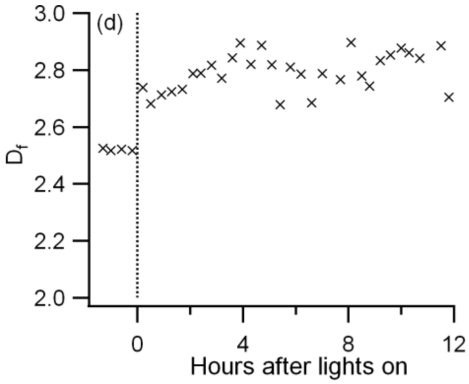

Figure 2.8 Fractal Dimension

It has been reported in Park et al. study that diesel at lower engine load of 10% has a fractal dimension of 2.41±0.02 and that at higher load of 75% is 2.33±0.03 (Park, 2003). Therefore, both Table 2.2 and Park's study shows a similar trend which suggests that particles are more compact at lower engine load. However, it is difficult to draw clear conclusion regarding the relationship between the fractal dimension and load because several other experimental conditions are also varied such as the dilution/injection method or the length of the transfer line.

In the atmosphere, the lifetime of volatile organic compounds depends on their rate of reaction with OH, NO_3 and O_3, which are the three most important oxidizing species in the air; hence, this is the reason why these compounds are being investigated in this study. NO_x significantly affects the pathways of reaction of the parent VOC by changing the fractions of the VOC reacting with OH, NO_3 and O_3, and also affecting various intermediate steps in the pathways (Seinfield, 2006). Indeed, one of the known important sources of OH radicals in the lower troposphere is the photolysis of O_3 in the presence of water vapor. However, according to Eq. 2.4 and Eq. 2.5, it is evident that the high NO concentration seen in the experiment suppresses the O_3 and NO_3 formation.

$$\mathbf{NO + O_3 \rightarrow NO_2 + O_2} \qquad \text{Eq. 2.4}$$

$$\mathbf{NO_2 + \frac{1}{3}O_3 \rightarrow NO_3} \qquad \text{Eq. 2.5}$$

As a result, only ethene plays a predominant role in reacting with OH radical; hence, the OH radical concentration can be predicted by the exponential decay of ethene concentration. The first order reaction representing the hydrogen abstraction between a hydroxyl radical and ethene to form a water molecule and an alkenyl radical is expressed in Eq. 2.6; the equation is derived from a pseudo-steady state assumption. By performing a curve fit of the exponential expression on the ethene concentration and with a known rate constant, the concentration of OH can be evaluated.

$$\mathbf{C(T) = C_0 exp(-k[OH]t)} \qquad \text{Eq. 2.6}$$

where C_0 *and C are ethene concentration initially and at time t, respectively, k is rate constant at room temperature using Arrhenius equation for ethene-OH reaction*

From such computation, the OH concentration is approximately 1-2x10^6 molecules cm^{-3}; this is approximately equivalent to 12 hours daytime average ambient OH concentration level (Atkinson, 2000). This is within reasonable agreement with the 3±1x10^6 molecules cm^{-3} OH concentration reported by another study (Weitkamp, 2007).

2.4 Discussion

2.4.1 Interpreting the formation of SOA

Volume measurements produce misrepresentation of SOA formation:

Figure 2.9 gives the output of the short transfer line, ejector-dilutor (Run 1) outputs. As can be seen, the particle volume concentration increased negligibly while the integrated mass concentration increased considerably right after the black lights is being turned on; this computation is done assuming minor wall-loss effect.

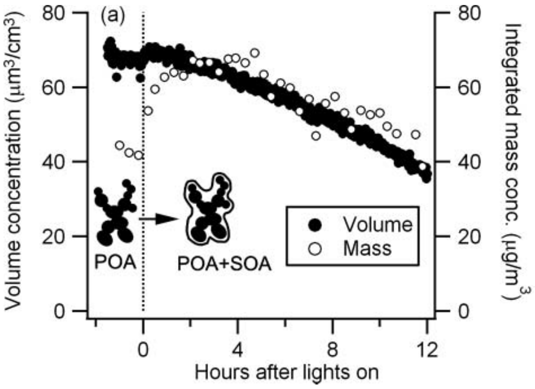

Figure 2.9 Particle volume concentration and mass concentration

With the increase in mass, it is beneficial to observe the effective density. It is observed that the effective densities as seen in Figure 2.10 increase rapidly from 30-80% of its initial value within the first two hours.

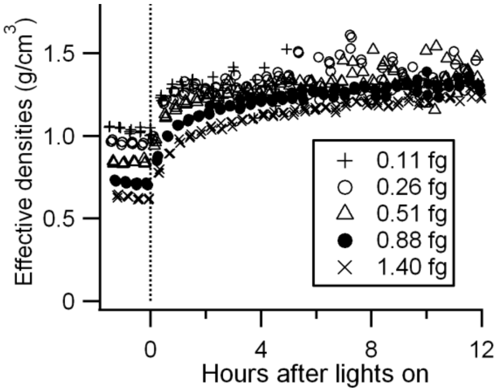

Figure 2.10 Effective density

Also, the VFR computed from the high temperature TD in Figure 2.11 remains fairly constant. Hence, it can be directly inferred that the changes in the mobility diameter is negligible since the VFR is highly dependent on the particles' diameter. However, this does not necessary mean that there are not many volatile components in the particulates.

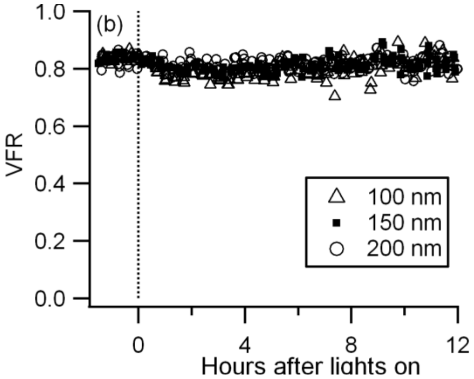

Figure 2.11 Volume fraction remaining

Indeed, even with the VFR trend in Figure 2.11, it is still expected that SVOCs must have evaporated by the TD. Hence, it is beneficial to observe the particle density before and after the TD as seen in Figure 2.12. The figure shows that the drop of density has clearly changed after the SOA formation, indicating the evaporation of SOA and leaving behind the fractal agglomerate backbone. However the little change in VFR can be associated with the increase in O/C ratio due to the condensation of more oxidized SOA.

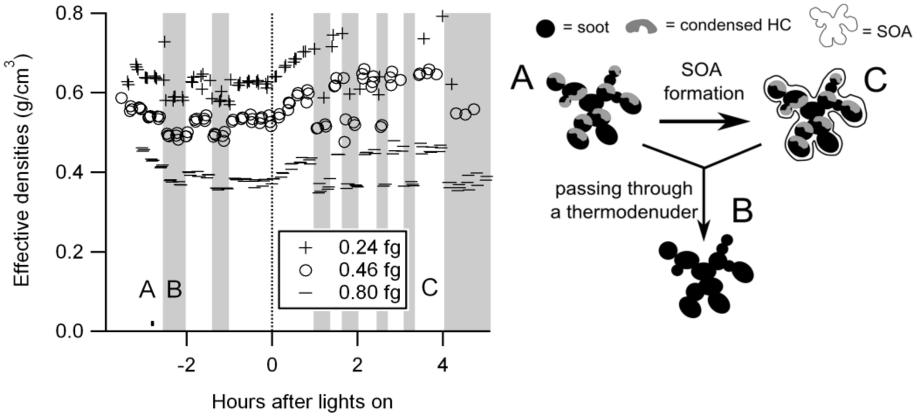

Figure 2.12 Time series of effective density of particles (Run 5). Shaded area indicates particles were passed through thermodenuder upstream of APM-SMPS

In summary, since both the effective density and mass concentration increase significantly but with minor changes in volume and VFR, this strongly suggests that SOA formation during the evolution process is used to fill the void space in the agglomerate particles (Figure 2.9-Figure 2.11). Since aging inside the environmental chamber causes condensation of secondary organics, the TD is placed in front of the APM-SMPS system to validate that the aged diesel particulates does indeed have organic condensing onto their fractal agglomerate backbone. As expected, since the TD stripes off all the volatiles components, the aged diesel particles after being heated through the TD is reported to have a much greater decrease in effective density as compared to the fresh diesel particulates (Figure 2.12). This shows that the reported minor volume concentration changes based on the mobility diameter is a misrepresentation of the chemistry of the aged diesel particle as it underestimate the OA formation and filling the void space.

AMS data supports the condensation of SOA:

It is apparent from Figure 2.13, which shows the HR-ToF-AMS measurements, that the oxygen to carbon ratio (O/C) rises continuously from 0.05 to 0.25 within 12 hours. From the increasingly oxidized nature of condensed-phase material (Weitkamp, 2007) and the rapid increase of oxygenate species after the black lights has been turned on indicates once again that there are condensation of secondary organics onto the diesel agglomerate.

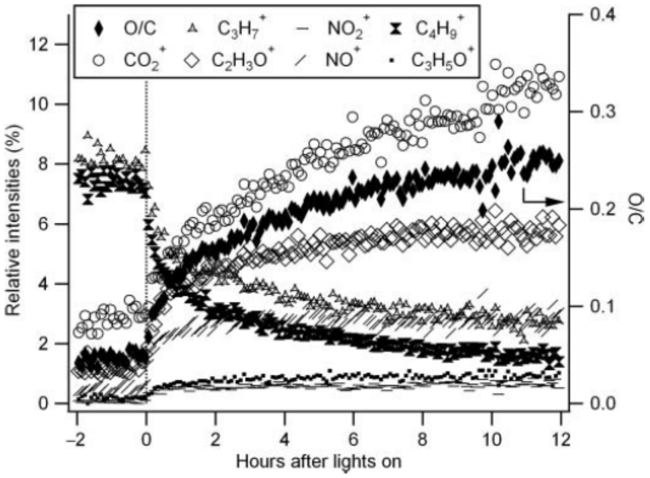

Figure 2.13 Time series of selected ions measured by an AMS for Run 1

This result is consistent with Sage's study on using an aerosol mass spectrometer to track the aging of diesel exhaust and to show that SOA are formed from atmospheric oxidation of a large suite of precursors at various pressures (Sage, 2008). They have found that the SOA through oxidation quickly approach a final mass spectrometry which closely resembles that of ambient aged organics. Similar to our study, Sage et al. has reported through the high resolution analysis that the organic mass indicative of oxidized material that appeared to be m/z=44 (CO_2^+) increases with time while m/z=57 ($C_4H_9^+$), which is associated with reduced organic material, decreases. These mass observations from current study and Sage et al. support the substantial formation of SOA from the oxidation of diesel emissions.

The condensation of SOA is also supported by Kroll's work which provided evidence that the cleavage of C-C bonds (fragmentation) is very critical in the formation of highly oxidized O/C organics from heterogeneous oxidation (Kroll, 2009). Such fragmentation produces volatile molecules which escape into the gas phase and decrease the carbon content of the particle. However, the oxygen containing functional groups add to the fragmentation sites of C-C bonds such that the oxygen content of the organics remains constant. As a result from Kroll's study, it can be concluded that the increase in O/C ratio in current study can potentially be driven not by the addition of oxygen but rather the loss of carbon.

MS before and after UV irradiation and its influence on SOA:

The aerosol mass spectrums of diesel exhaust particulate before and after UV irradiation is obtained with the HR-ToF-AMS as shown in Figure 2.14. The results of the significant increase in m/z=30 (NO^+ fragment) and negligible ammonium ion are supportive of the possibility that the high NO_x concentration applied in this current work has led to the formation of organic nitrogen containing species.

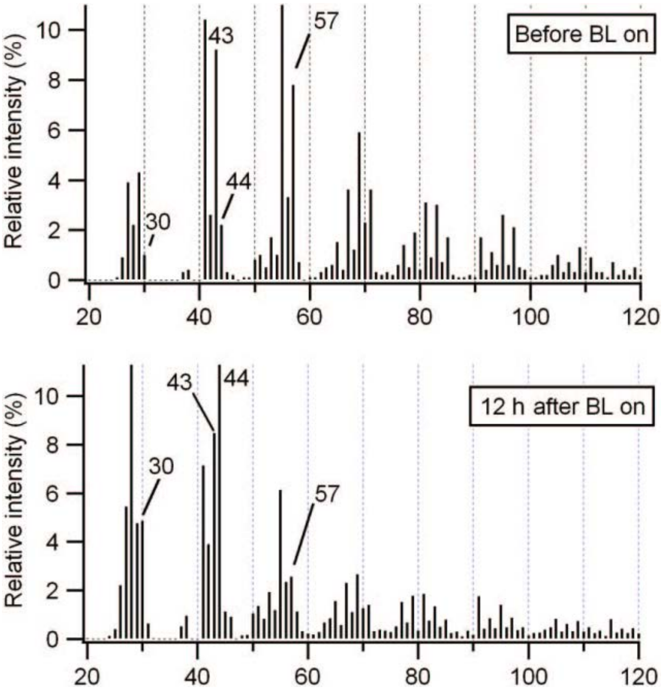

Figure 2.14 Mass spectrums obtained before and after UV irradiation for Run 1

Previous studies (Chirico, 2010) have used Eq. 2.7 to estimate the formation of SOA during the evolution inside the environmental chamber with a diesel power generator. This is done by subtracting the initial non-oxygenated organic matter (OM) mass, which is the primary organic aerosol, from the total OM at any indicated time.

$$\%\mathbf{SOA}(\mathbf{t}) = \left[\mathbf{Org}(\mathbf{t}) - \frac{\mathbf{C_4H_9^+(t)}}{\mathbf{C_4H_9^+(t_0)}}\mathbf{xOrg}(\mathbf{t_0})\right]/\mathbf{Org}(\mathbf{t}) \qquad \text{Eq. 2.7}$$

where Org(t) is the measured total OM concentration at time t, $C_4H_9^+(t)$ *is the non-oxygenated fragment at m/z 57,* $C_4H_9^+(t_0)$ *is the non-oxygenated at m/z 57, and Org(*t_0*) is the OM concentration at time t=0 which is before the black lights are turned on.*

It is very common that m/z 57 is predominantly associated with primary species that comes from long-chain alkyl group ($\mathrm{C_4H_9^+}$), which has been found to be one of the dominant ions in the mass spectrum of organic aerosols from diesel engines (Schauer, 1999). In present study, Eq. 2.7, which has been suggested by Sage et al., is preferred over the method of subtracting the initial OM mass of POA from the total OM at time t using the high resolution W-mode of the AMS. In Sage's study, it was assumed that the m/z 57 is predominantly from primary species that is in the form of $\mathrm{C_4H_9^+}$ and the m/z 57 ratio of primary organic aerosol remained constant during the evolution process inside the smog chamber. However, it has been discovered that the ions containing oxygen, especially $C_3H_5O^+$, does contributes heavily to the mass of m/z 57 signal (DeCarlo, 2006). At the beginning when the black lights are turned on, the $\mathrm{C_4H_9^+}$ takes up the major fraction of the signal at m/z 57. But after 12 hours of irradiation, the relative fraction of $C_3H_5O^+$ at m/z 57 increases with time, which has been shown to become more prominent for experiment that has high SOA production (Chirico, 2010). From such observation, it can be concluded that the method suggested in Sage et al. will overestimate the POA concentration and underestimate the SOA formation during the aging process since it assigned all the m/z 57 as primary particles. Therefore in this study, $C_4H_9^+$ has been selected as the tracer rather than just the initial organic mass by utilizing the high resolution capability of HR-ToF-AMS. Hence, Eq. 2.7 is a more accurate approach to compute the SOA formation by substituting m/z 57 with specifically non-oxygenated fragment.

By applying Eq. 2.7, it is possible to estimate the fraction of secondary organic aerosols (SOA) and primary organics aerosol (POA) in the total organics, which is depicted in Figure 2.15. The figure shows that the estimated SOA fraction is 50% within the first 2-4 hours of irradiation, and 80% of total organic aerosol in half a day (12 hours).

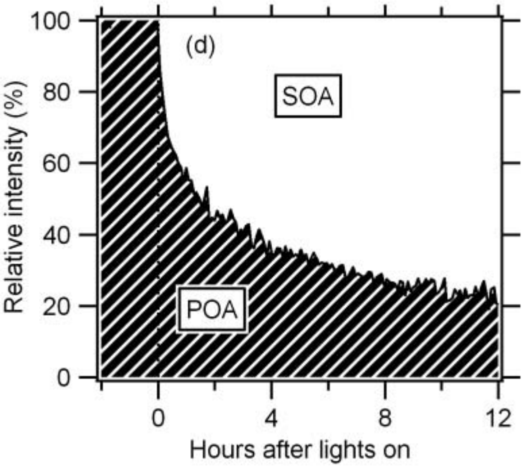

Figure 2.15 Fraction of Organic Aerosols

2.4.2 Interpreting the effect of the dilution/injection method on the particulates' evolution inside the chamber

The impact of various dilution methodologies and the length of the transfer line as discussed in section 2.2.3 with a focus on the physical evolution of the particles inside the environmental chamber will be investigated in this section. Specifically, the particle volume, mass concentration, and bulk effective density in different experimental conditions are investigated.

Influences on bulk effective densities from different dilution ratios and methods:

The bulk effective densities are calculated by integrating the mass and volume concentration after the completion of the injection. When diesel engines are operated on medium loads, the elemental carbon/soot dominates over the SVOCs and, thus, dilution will have minor impact on the diesel particulates (Lipsky, 2006). This is confirmed in Figure 2.16 (runs 6,7,8,11,12) because as the exhaust particulates are diluted under controlled experimental condition (16 m long transfer line under medium load condition), it is apparent that the bulk effective densities are not a function of the dilution ratios.

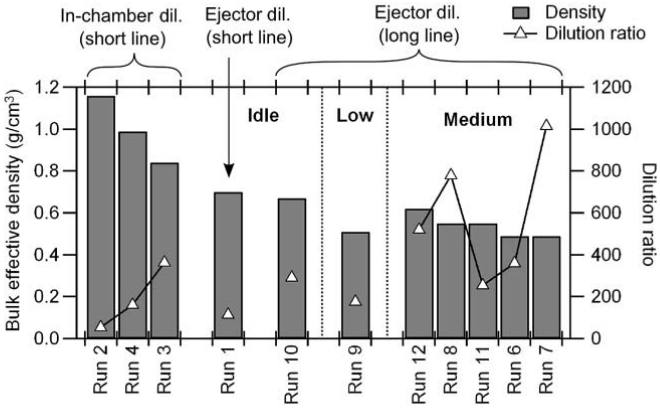

Figure 2.16 Effective densities of particles in an environmental chamber and dilution ratio when the injection was completed

On the other hand, under the idling condition in runs 1-4, the dilution methods attribute significantly to bulk effective densities of the particles. The particle density is observed to be significantly higher (12-55%) when the raw exhaust (run 2-4) is injected into the chamber than when diluted exhaust is injected (run 1) as seen from Figure 2.17. However, it is also known that the initial particle density is expected to depend on dilution ratio of the exhaust due to the repartitioning of condensed semi-volatile hydrocarbon compounds (SVOCs) in POA. Therefore, it is necessary to investigate whether this trend can be explained solely by dilution ratio or methods.

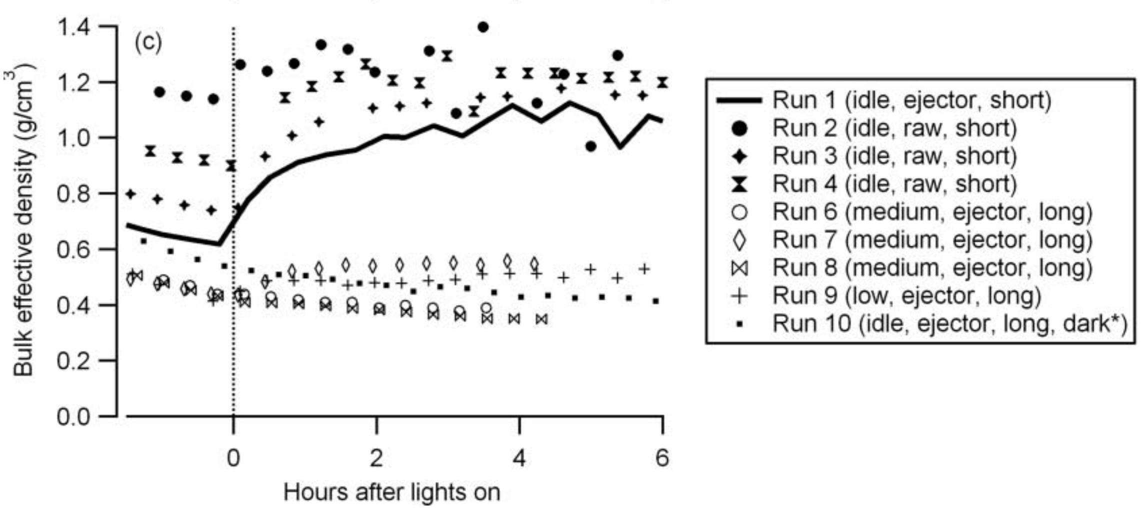

Figure 2.17 Evolution of bulk effective density

As seen from Table 2.2, the dilution ratio in run 1 is smaller than run 3-4 but the bulk effective density of run 1 remains lower. This proves that dilution ratio by itself cannot account for the lower density in run 1. Also, it can be seen that there are no systematical ways to relate the initial particle size dependence of density by solely looking at the dilution ratio. Indeed, a closer look suggests that the violent dilution leading to vigorous turbulent employed by the ejection-dilution system helps the low volatile compounds on the particulates to evaporate in a shorter time scale when compared to the stagnant dilution of the raw exhaust plume injection. The method of filling the empty chamber with an exhaust sampling line that has been diluted with highly compressed air from the ejector might leads to faster evaporation of the semivolatiles than the relatively stagnant method of plume injection into a chamber that have already been filled with air.

This similar effect has been observed in Lipsky's study where an evaporation timescale of 2.5 s had been found for diesel particulates in a dilution sampler that induced turbulent mixing (Lipsky 2005). Grieshop et al studied unburned lubricating oil as it is one of the dominant components of diesel emission. In their experiment, lubricating oil aerosol was generated by flash vaporizing and used SAE 10W-30 oil at 425°C (Grieshop, 2009). On contrary to Lipsky et al. reported timescale, it was found from Grieshop et al. in-chamber dilution experiment that the lubrication oil aerosols had an evaporation timescale in the order of hours. The slow evaporation was unlikely due to particles lost to the chamber walls since the delay in evaporation of wall-bound particles would have a tendency to depress the vapor concentrations and consequently caused an increase in evaporation rates.

Therefore, results from both Grieshop et al. and Lipsky et al. regarding such dilution characteristic is also observed in this current study. Hence, it is suggested that the kinetics of evaporation of SVOCs are inhibited by strong adsorption and it is necessary to apply turbulent dilution to overcome the kinetics for possible desorption of the SVOCs from the fractal agglomerates.

In Figure 2.17 there is an interesting observation that although runs 7-9 are under the same load and are diluted in a long transfer line, the density in runs 7 and 9 shows a clear increase while that of runs 6 and 8 decreases slightly after the light is turned on. This can be potentially associated with a high SOA formation rate in runs 7 and 9 and a minor one for runs 6 and 8. However, the reason for such difference is still not aware of since runs 6-9 have similar experimental conditions. Furthermore, it is apparent from Figure 2.17 that there is not much aerosol growth in those experiments with longer transfer lines (runs 6-9). However, it might not be related to the length of the transfer line. It is hypothesized that the difference can be ascribed to the engine load condition in runs 1-4, which results in higher SOA formation due to higher semi-volatile emission when engine is idling and from cold start.

Impact on volume and mass concentration under different dilution conditions:

It has been observed that the particle volume concentrations increase in the dark regardless of engine load and length of transfer lines. The only plausible ways for the volume to increase is either from coagulation or condensation. Since the diesel particle are fractal, the condensation of SVOCs will make the particles more dense by filling the void space rather than increasing the mobility diameter as observed in Figure 2.18. Hence, that leaves with the only possible reason for such behavior to be associated with coagulation. Coagulations leading to less dense particles will occur regardless of experimental conditions. Furthermore, as confirmed through this work, the diesel particles are fractal-like agglomerates. Coagulation between fractal particles leads to accumulation into agglomerates chains with a lot of void spaces causing the particles to become less dense. This is consistent with the trend in Figure 2.18.

Additionally, it is observed that the test conditions (runs 6-12), which show an increase in the volume concentration before the light is turned on, correlates with lower particle effective bulk densities than the other reported conditions. Thus, it can be concluded that if the particles have lower effective density to begin with, there will be more frequent coagulations. However, runs 1 and 10 in Figure 2.18 show an exception of a minor density differences (as seen in Figure 2.17) but significant difference in volume evolution. Although the exact explanation for this volume trend is not available at this moment, this once again serves as a good case to emphasize on the importance of mass-based measurement in diesel chamber study.

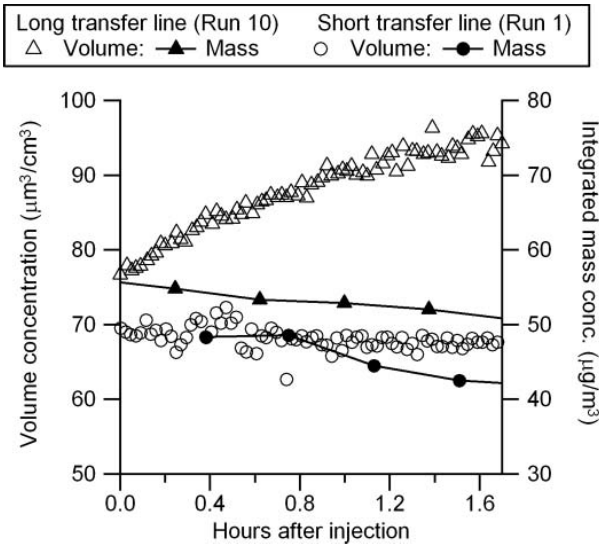

Figure 2.18 Comparison of short and long transfer line concentrations before lights are turned on

Interpreting SOA formation at different dilution conditions:

The evolution of primary organic aerosol (POA) fraction in Figure 2.19 can be computed by using the AMS $C_4H_9^+$ tracer method under various loads (idle, low, medium), injection methods (ejector dilution, in-chamber dilution), and transfer lines (2 m, 16 m).

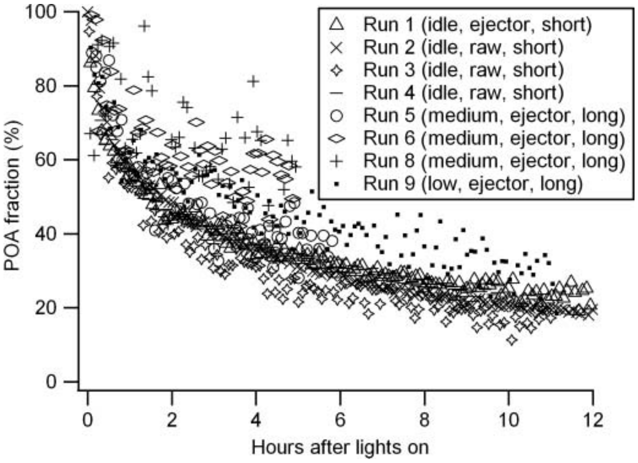

Figure 2.19 Evolution of primary organic aerosol fraction

The overall trend shows a rapid decrease in the POA fraction as a result from SOA formation. It can be interpreted for the majority of the runs that there are no significant systematic differences in POA fractions from aerosol aging due to the load or injection method. This suggests that the varying particle volume concentration and bulk effective density for the different experimental conditions is primarily due to the evolution of physical structures of the particle as opposed to the chemical components inside the chamber. However, runs 6 and 8 do portrays a higher POA fraction than the other runs, indicating a lower SOA fraction. Since, according to Figure 2.17, the effective densities of these two systems decrease after the lights are turned on, it is expected that the SOA fractions will be smaller as indicated in Figure 2.18. However, the AMS MS for runs 6 and 8 still looks similar to those from other runs after 12 hours of oxidation; they all show substantial SOA formation since the MS included m/z 30, 41, 43, 44, 55, and 57. Due to experimental, run-to-run variability, it is not apparent whether the effect of transfer line length can be attributed to the difference in SOA formation for runs 6 and 8 when compared to the others.

Conclusion

In this research work, secondary organic aerosols (SOA) are produced from a diesel exhaust and are diluted before being transferred into an environmental chamber with UV irradiation. There are two dilution techniques of interest:

1) A rapid ejector dilutor system

2) A stagnant in-chamber dilution

The effective densities from the in-chamber dilution of injecting raw exhaust into an air filled chamber is higher than those from the ejector dilutor where diluted exhaust are injected into an empty chamber. The faster evaporation of SVOCs in the ejector dilutor system is due to the intense mixing of raw exhaust with pressurized compressed air. Filling an empty bag with diluted exhaust can leads to enhanced turbulence during the bag filling process which is also responsible for the greater evaporation behavior. This highly suggests that the dilution ratio as well as dilution method play a significant impact on the evaporation rate of SVOCs, and therefore, SOA evolution inside the environmental chamber.

It is found that the volumetric concentrations that are solely based on mobility diameter underestimate the SOA formation due to the agglomerates' external void space. Thus, due to the fractal nature of SOA, it is necessary to run a particle mass analysis in order to accurately interpret SOA evolution from a diesel exhaust. Hence, the APM-SMPS is employed to determine the particle effective density, which in turn can output the mass concentration through computation. This will gives a better understanding of

SOA evolution by generating more accurate measurements of the particle mass concentration and fractal dimension.

The reported oxygen to carbon ratio (O/C) from the HR-ToF-AMS measurement has shown to increase during the continuous aging of 12 hours of oxidation under the UV irradiation inside the environmental chamber. The instrument also shows that 50% of the organic aerosol is composed of SOA during the first 2-5 hours of photo-oxidation and the SOA fraction increases up to 80% of the organic mass within 12 hours. This gives a clear indication that the multigenerational oxidation of low-volatile organic vapors from diesel emission contributes significantly to the formation of ambient oxygenated SOA in urban area.

References

Aiken, A. C., DeCarlo, P. F., Kroll, J. H., Worsnop, D. R., Huffman, J. A., Docherty, K., Ulbrich, I., Mohr, C., Kimmenl, J. R., Sun, Y., Zhang, Q., Trimborn, A. M., Northway, M., Ziemann, P. J., Canagaratna, M. R., Onasch, T. B., Alfarra, M. R., Prevot, A. S., Dommen, J., Duplissy, J., Metzger, A., Baltensperger, U., Jimenez, J. L., 2008. O/C and OM/OC ratios of primary, secondary, and ambient organic aerosols with High-Resolution Time-of-Flight Aerosol Mass Spectrometry. Environmental Science & Technology

Arey, J., Obermeyer, G., Aschmann, S. M., Chattopadhyay, S., Cusick, R. D., Atkinson, R., 2009. Dicarbonyl products of the OH radical-initiated reaction of a series of aromatics hydrocarbons. Environmental Science & Technology.

Atkinson, R.: Atmospheric chemistry of VOCs and NOx, Atmospheric Environment, 34, 2063-2101, 2000

Cai, X., Ziemba, L. D., Griffin, R. J., 2008. Secondary aerosol formation from the oxidation of toluene by chlorine atoms. Atmospheric Environment 42, 7348-7359

California Air Resources Board. *California Regional Haze Plan 2014 Progress Report* [http://www.arb.ca.gov/planning/reghaze/progress/carhpr2014.pdf]

Calvert, J. G., Atkinson, R., Becker, K. H., Kamens, R. M., Seinfeld, J. H., Wallington, T. J., Yarwood, G., 2002. The mechanism of atmospheric oxidation of aromatics hydrocarbons, Oxford University Press.

Cao, G., Jang, M., 2010. An SOA model for toluene oxidation in the presence of inorganic aerosols. Environmental Science & Technology.

Chan, C.C. Modern Electric Vehicle Technology. New York: Oxford University Press Inc, 2007. Print.

Chan, A. W. H., Kautzman, K. E., Chhabra, P. S., Surratt, J. D., Chan, M. N., Crounse, J.D., Kurten, A., Wennberg, P. O., Flagan, R. C., Seinfeld, J. H.: Secondary organic aerosol formation from photooxidation of naphthalene and alkylnaphthalenes: implications for oxidation of intermediate volatility organic compounds (IVOCs), Atmospheric Chemistry and Physics, 9, 3049-3060, 2009

Chen, D. R.; Pui, D. Y. H.; Hummes, D.; Fissan, H.; Quant, F. R.; Sem, G. J. Design and evaluation of a nanometer aerosol differential mobility analyzer (Nano-DMA). *J. Aerosol Sci.* **1998**, *29* (5-6), 497–509.

Chirico, R., DeCarlo, P. F., Heringa, M. F., Tritscher, T., Richter, R.,Dommen, J., Weingartner, E., Wehrle, G., Gysel, M., Laborde, M., Baltensperger, U.: Impact of aftertreatment devices on primary emissions and secondary organic aerosol formation potential from in-use diesel vehicles: results from smog chamber experiments, Atmos. Chem. Phys., 10(23), 11545-11563, 2010

Choo, J.; Jung, J.; Kim, W.; Oh, H.; Kim, J.; Kim, H.; Kim, Y.; Kim, S. Oxidation characteristics of airborne carbon nanoparticles by NO2. *Sci. Total Environ.* **2008**, *405* (1/3), 396–401.

Claire, S. Born Under a Bad Sky. Dissident Voice, 2004.

Davidson, C. I., Phalen, R. F., Solomon, S.: Airborne particulate matter and human health: A review, Aerosol Science and Technology, 39, 737-749, 2005

DeCarlo, P. F., Kimmel, J. R., Trimborn, A., Northway, M. J., Jayne, J. T., Aiken, A. C., Gonin, M., Fuhrer, K., Horvath, T., Docherty, K. S., Worsnop, D. R., and Jimenez, J. L.: Field-deployable, high-resolution, time-of-flight aerosol mass spectrometer, Anal. Chem., 78, 8281–8289, 2006.

Ehrburger, P. B. J.; Drouillot, Y.; Logie, V.; Gilot, P. Reactivity of Soot with Nitrogen Oxides in Exhaust Stream; *SAE Tech. Pap. Ser.* **2002**, *No 2002-01-1683*.

EPA. Health assessment document for diesel engine exhaust. Technical report, 2002.

Felton, M. The Clean Air Act Targets Engine Emissions. [cited; Available from: http://pubs.acs.org/subscribe/archive/tcaw/10/i04/html/TCAW04regs.html]

GÃijnter OberdÃ″urster, Z. Sharp, V. Atudorei, A. Elder, R. Gelein, W. Kreyling, and C. Cox. Translocation of inhaled ultrafine particles to the brain. Inhalation Toxicology, 16(6-7):437–445, 2004.
Grieshop, A. P., Miracolo, M. A., Donahue, N. M., Robinson, A. L.: Constraining the volatility distribution and gas-particle partitioning of combustion aerosols using isothermal dilution and thermodenuder measurements, Environmental Science & Technology, 43(13), 4750-4756, 2009.

Grieshop, A. P.,Miracolo, M. A., Donahue, N. M., and Robinson, A. L. (2009). Constraining the Volatility Distribution and Gas-Particle Partitioning of Combustion Aerosols Using Isothermal Dilution and Thermodenuder Measurements. *Environ. Sci. Technol.*, 43(13):4750–4756.

Hallquist, M., Wenger, J.C., Baltensperger, U., Rudich, Y., Simpson, D., Claeys, M., Dommen, J., Donahue, N.M., George, C., Goldstein, A.H., Hamilton, J.F, Herrmann, H., Hoffmann, T., Iinuma, Y., Jang, M., Jenkin, M., Jimenes, J.L., Kiendler-Scharr, A., Maenhaut, W., McFiggans, G., Menteol, T.F., Monod, A., Prevot, A.S., Seinfield, J.H., Suratt, J.D., Szmigielski, R., Willdt, J., 2009. The formation, properties and impact of secondary organic aerosol: current and emerging issues. Atmopsheric Chemistry and Physics 9, 5155-5236.

Hansen, J. and L. Nazarenko, Soot climate forcing via snow and ice albedos PNAS, 2004. **101**(2): p. 423-428.

Higgins, K. J.; Jung, H.; Kittelson, D. B.; Roberts, J. T.; Zachariah, M. R. Size-selected nanoparticle chemistry: Kinetics of soot oxidation. *J. Phys. Chem. A* **2002**, *106* (1), 96–103.

Higgins, K. J.; Jung, H.; Kittelson, D. B.; Roberts, J. T.; Zachariah, M. R. Kinetics of diesel nanoparticle oxidation. *Environ. Sci. Technol.* **2003**, *37* (9), 1949–1954.

Jacquot, F.; Brilhac, J. F. Soot Oxidation by O2 and/or NO2 in the Presence of Catalysts under Lean-Burn and Rich Atmospheres. *SAE Tech. Pap. Ser.* **2004**, *No 2004-01-1943*.

Jayne J.T., Leard D.C., Zhang X., Davidovits P., Smith K.A., Kolb C.E., Worsnop D.R., Development of an aerosol mass spectrometer for size and composition analysis of submicron particles**.** *Aerosol Sci. Technol*., 33, 49-70, 2000.

Johnson, D., Jenkin, M. E., Wirtz, K., Martin-Reviejo, M., 2005. Simulating the formation of secondary organic aerosol from the photooxidation of aromatics hydrocarbons. Environ. Chem. 2, 35-48.

Lahde, T., Ronkko, T., Virtanen, A., Schuck, T.J., Pirjola, L.,Hameri, K., Kulmala,M., Arnold, F., Rothe, D., Keskinen, J. Heavy duty diesel engine exhaust aerosol particle and ion measurements. Environmental
Science & Technology, 43(1):163–168, 2009.

Khalek, I. A., Kittelson, D. B., and Brear, F. (2000). Nanoparticle Growth During Dilution and Cooling of Diesel Exhaust: Experimental Investigation and Theoretical Assessment. *SAE Technical Paper Series,* 2000-2001-0515.

Kamm, S.; Saathoff, H.; Naumann, K. H.; Mo¨hler, O.; Schurath, U. Gasification of a soot aerosol by O3 and NO2: Temperature dependence of the reaction probability. *Combust. Flame* **2004**, *138* (4), 353–361.

Kanakidou, M., Seinfeld, J. H., Pandis, S. N., Barnes, I., Dentener, F. J., Facchini, M. C., Van Dingenen, R., Ervens, B., Nenes, A., Nielsen, C. J., Swietlicki, E., Putaud, J. P., Balkanski, Y., Wilson, J.: Organic aerosol and global climate modelling: a review, Atmospheric Chemistry and Physics, 5, 1053-1123, 2005

Kittelson, D.B., Engines and nanoparticles: a review. Journal of Aerosol Science, 29(5-6):575–588, 1998.

Kroll, J. H., Seinfeld, J. H., 2008. Chemistry of secondary organic aerosol: Formation and evolution of low-volatility organics in the atmosphere. Atmospheric Environment.

Kroll, J. H., Smith, D. F., Che, D. L., Kessler, S. H., Worsnop, D. R., and Wilson, K. R. (2009). Measurement of Fragmentation and Functionalization Pathways in the Heterogeneous Oxidation of Oxidized Organic Aerosol. *Phys. Chem. Chem. Phys.*, 11:8005–8014.

LINDBERG/BLUE M, "*Catalog of tube furnace HTF55122A"*

Lipsky, E.M., and Robinson, A. L. (2005). Design and Evaluation of a Portable Dilution Sampling System for Measuring Fine Particle Emissions from Combustion Systems. *Aerosol Sci. Technol.*, 39:542–553.

Ma, H.; Jung, H.; Kittelson, D. B. Investigation of diesel nanoparticle nucleation mechanisms. *Aerosol Sci. Technol.* **2008**, *42* (5), 335–342.

Malloy, Q., Nakao, S., Qi, L., Austin, R. L., Stothers, C., Hagino, H., Cocker, D. R.: Real-time aerosol density determination utilizing a modified Scanning Mobility Particle Sizer - Aerosol Particle Mass Analyzer system, Aerosol Science and Technology, 43, 673-678, 2009

Marcuccilli, F.; Gilot, P.; Stanmore, B.; Prado, G. Experimental and theoretical study of diesel soot reactivity. *Combust. Inst.,Twenty-fifth Symp. (Int.) on Combust.* **1994**, 619–626.

McMurry, P. H., Wang, X. W., Park, K., Ehara, K.: The relationship between mass and mobility for atmospheric particles: A new technique for measuring particle density,Aerosol Science and Technology, 36, 227-238, 2002

M. Matti Maricq. Chemical characterization of particulate emissions from diesel engines: A review. Journal of Aerosol Science, 38(11):1079–1118, 2007.

Muckenhuber, H.; Grothe, H. The heterogeneous reaction between soot and NO2 at elevated temperature. *Carbon* **2006**, *44* (3), 546–559.

Muckenhuber, H.; Grothe, H. A DRIFTS study of the heterogeneous reaction ofNO2 with carbonaceous materials at elevated temperature. *Carbon* **2007**, *45* (2), 321–329.

Marques, R.; Darcy, P.; Da Costa, P.; Mellottee, H.; Trichard, J. M.; Djega-Mariadassou, G. Kinetics and mechanism of steadystate catalytic NO+O-2 reactions on Pt/SiO2 and Pt/CeZrO2. *J. Mol. Catal A: Chem.* **2004**, *221* (1-2), 127–136.

Neil,A., Xia T., Madler, L., Li, N., 2006. Toxic potential of materials at the nanolevel. Science 311, 622-627.

Nienow, A. M.; Roberts, J. T.; Zachariah, M. R. Surface chemistry of nanometer-sized aerosol particles: Reactions of molecular oxygen with 30nm soot particles as a function of oxygen partial pressure. *J. Phys. Chem. B* **2005**, *109* (12), 5561–5568.

Odum J.R., Jungkamp, T.P.W, Griffin,R.J., Forstner, H.J.L., Flagan, R.C., Seinfeld, J.H., (1997a) The atmospheric aerosol-forming potential of whole gasoline vapor, *Science* **276** 96-99.

Olariu, R. I., Klotz, B., Barnes, I., Becker, K. H., Mocanu, R., 2002. FT-IR study of the ring-retaining products from the reaction of OH radicals with phenol, o-, m-, and p-cresol. Atmospheric Environment 36, 3685-3697.

Park, J.; Giles, N. D.; Moore, J.; Lin, M. C. A comprehensive kinetic study of thermal reduction ofNO2 by H-2. *J. Phys. Chem. A* **1998**, *102* (49), 10099–10105.

Park, K., Kittelson, D. B., McMurry, P. H.: Relationship between particle mass and mobility for diesel exhaust particles, Environmental Science & Technology, 37(3), 577-583, 2003

Pope, C.A, Young B., Dockery, D. W.. Health effects of fine particulate air pollution: lines that connect. Journal of the Air &Waste Management Association, 56(6):709–742, 2006.

Rahman, S. Bradley, V. Shrestha, G.B et al, 2002. An investigation into the impact of electric vehicle load on the electric utility distribution system. Power Delivery, IEEE Transactions, Volume:8, Issue 2, 591-597.

Robinson, A. L., Donahue, N. M., Shrivastava, M. K., Weitkamp, E. A., Sage, A. M., Grishop, A. P., Lane, T. E., Pierce, J. R., Pandis, S. N.: Rethinking organic aerosols: Semivolatile emissions and photochemical aging, Science, 315, 1259-1262, 2007

Samy, S., Zielinska, B.: Secondary organic aerosol production from modern diesel engine emission, Atmospheric Chemistry and Physics, 10, 609-625, 2010

Sage, A. M., Weitkamp, E. A., Robinson, A. L., and Donahue, N. M. (2008). Evolving Mass Spectra of the Oxidized Component of Organic Aerosol: Results from Aerosol

Mass Spectrometer Analyses of Aged Diesel Emissions. *Atmos. Chem. Phys.*, 8:1139–1152.

Schauer, J. J., Rogge, W. F., Hildemann, L. M., Mazurek, M. A., Cass, G. R.: Source apportionment of airbourne particulate matter using organic compounds as tracers, Atmospheric Environment, 30(22), 3837-3855, 1996

Schauer, J. J., Kleeman, M. J., Cass, G. R., and Simoneit, B. R. T.: Measurement of emissions from air pollution sources. 2. C1 through C30 organic compounds from medium duty diesel trucks, Environ. Sci. Technol., 33, 1578–1587, 1999.

Seinfield, J., Spyros, P. *Atmospheric Chemistry and Physics.* New Jersey: John Wiley & Sons, Inc, 2006. Print

Setiabudi, A.; Makkee, M.; Moulijn, J. A. The role of NO2 and O-2 in the accelerated combustion of soot in diesel exhaust gases. *Appl. Catal., B* **2004**, *50* (3), 185–194.

Somers, C.M,, McCarry, B.E., Malek, F., Quinn, J.S., 2004. Science 304, 1008-1010.

Stanmore, B. R., Brillac, J. R.,Gilot, P. The oxidation of soot: a review of experiments, mechanisms and models. Carbon 2001, 39, 2247-2268.

Strader R., Lurnmann,F., Pandis,S.N. (1999) Evaluation of secondary organic aerosol oration in winter, *Atmos. Environ.* **33** 4849-4863.

Shrivastava, M.; Gidwani, A.; Jung, H. Modeling oxidation of soot particles within a laminar aerosol flow reactor using computational fluid dynamics. *Aerosol Sci. Technol.* **2009**, *43* (12), 1218–1229.

Shrivastava, M., Nguyen A., Zheng, Zhongqing., Wu H., Jung, H., Kinetics of Soot Oxidation by NO_2. Environ. Sci. Technol. 2010, *44* (12), pp 4796–4801

Sydbom, A., Blomberg, A., Parnia, S., Stenfors, N., Sandstrom, T., Dahlen, S.E., 2001. Health effects of diesel exhaust emissions. European Respiratory Journal 17, 733-746.

Takekawa, H., Minoura, H., Yamazaki, S., 2003. Temperature dependence of secondary organic aerosol formation by photo-oxidation of hydrocarbons. Atmospheric Environment 37, 3413-3424.

Volkamer, R., Klotz, B., Barnes, I., Imamura, T., Washida, N., 2002. OH-initiated oxidation of benzene Part 1. Phenol formation under atmospheric conditions. Phys. Chem. Chem. Phys. 4, 1598-1610.

Weitkamp, E. A., Sage, A. M., Pierce, J. R., Donahue, N. M., Robinson, A. L.: Organic aerosol formation from photochemical oxidation of diesel exhaust in a smog chamber, Environmental Science & Technology, 41(20), 6969-6975, 2007

Wehner, B., Uhrner, U., Von Lowis, S., Allinger M., Wiedensohler, A., 2009. Aerosol number size distribution within the exhaust plume of a diesel and a gasoline passenger car under on-road conditions and determination of emission factors. Atmospheric Environment 43, 1235-1245.

Wu, Y., Hao, J.M., et al., 2002. Vertical and horizontal profiles of airborne particulate matter near major roads in Macao, China. Atmospheric Environment 36 (31), 4907–4918.

Xue, H., Khalizov, A. F., Wang, L., Zheng, J., Zhang, R.: Effects of coating of dicarboxylic acids on the mass-mobility relationship of soot particles, Environmental Science & Technology, 43, 2787-2792, 2009

Zhang, K.M., Wexler, A.S., et al., 2004. Evolution of particle number distribution near roadways. Part II: the ‘Road-to-Ambient’ process. Atmospheric Environment 38 (38), 6655–6665.

Zhang, J., 2010. Diesel Emission Technology-Part II of Automotive After-Treatment System.
[cited; Available from: www.bowmannz.com]

Zhu, Y.F., Hinds, W.C., et al., 2002. Concentration and size distribution of ultrafine particles near a major highway. Journal of the Air & Waste Management Association 52 (9), 1032–1042.